ARTICLE IN PRESS

Communications Physics

https://doi.org/10.1038/s42005-026-02495-w

Article in Press

Optimal coloring and strain-enhanced superconductivity in $Li_nB_{n+1}C_{n-1}$

Received: 19 May 2025

Accepted: 6 January 2026

Cite this article as: Gu, Y., Hu, J., Jiang, H. *et al.* Optimal coloring and strain-enhanced superconductivity in $Li_nB_{n+1}C_{n-1}$. *Commun Phys* (2026). https://doi.org/10.1038/s42005-026-02495-w

Yuhao Gu, Jiangping Hu, Hong Jiang & Tao Xiang

We are providing an unedited version of this manuscript to give early access to its findings. Before final publication, the manuscript will undergo further editing. Please note there may be errors present which affect the content, and all legal disclaimers apply.

If this paper is publishing under a Transparent Peer Review model then Peer Review reports will publish with the final article.

ARTICLE IN PRESS

© The Author(s) 2026. **Open Access** This article is licensed under a Creative Commons Attribution-NonCommercial-NoDerivatives 4.0 International License, which permits any non-commercial use, sharing, distribution and reproduction in any medium or format, as long as you give appropriate credit to the original author(s) and the source, provide a link to the Creative Commons licence, and indicate if you modified the licensed material. You do not have permission under this licence to share adapted material derived from this article or parts of it. The images or other third party material in this article are included in the article's Creative Commons licence, unless indicated otherwise in a credit line to the material. If material is not included in the article's Creative Commons licence and your intended use is not permitted by statutory regulation or exceeds the permitted use, you will need to obtain permission directly from the copyright holder. To view a copy of this licence, visit http://creativecommons.org/licenses/by-nc-nd/4.0/.

ARTICLE IN PRESS

Optimal coloring and strain-enhanced superconductivity in $Li_nB_{n+1}C_{n-1}$

Yuhao Gu,[1] Jiangping Hu,[2,3,4,*] Hong Jiang,[5,†] and Tao Xiang[2]

[1]*School of Mathematics and Physics, University of Science and Technology Beijing, Beijing 100083, China*

[2]*Institute of Physics, Chinese Academy of Sciences, Beijing 100190, China*

[3]*Kavli Institute of Theoretical Sciences, University of Chinese Academy of Sciences, Beijing, 100190, China*

[4]*New Cornerstone Science Laboratory, Beijing 100190, China*

[5]*Beijing National Laboratory for Molecular Sciences, College of Chemistry and Molecular Engineering, Peking University,Beijing 100871, China*

ARTICLE IN PRESS

Abstract

Boron-rich lithium borocarbides are promising candidates for phonon-mediated high-temperature superconductors due to their metallic σ-bonding electrons. Here, we use the cluster expansion method to identify energetically stable configurations (colorings) of Li_2B_3C and $Li_3B_4C_2$, which are characterized by a distinctive pattern of alternating B-B and B-C zigzag chains. Surprisingly, the optimal configuration of Li_2B_3C exhibits an extremely low superconducting transition temperature of $T_c < 0.03$ K, which is attributed to the suppression of deformation potentials near the Fermi level caused by the specific electron filling of B-B zigzag chains. However, the σ-bonding electrons at the Fermi level are highly sensitive to external strain or pressure. Specifically, applying a -5% compressive uniaxial strain can significantly enhance the electron-phonon coupling and the Eliashberg spectral function, boosting up T_c to 37 K. This work not only presents a strategy for achieving high critical temperatures in $Li_nB_{n+1}C_{n-1}$ compounds, but also provides valuable insights into the complex interplay between electronic structure and superconducting interaction.

* jphu@iphy.ac.cn

† jianghchem@pku.edu.cn

ARTICLE IN PRESS

I. INTRODUCTION

The allure of high-temperature superconductivity continues to fascinate the scientific community worldwide. The metallization of strong chemical bonding electrons is considered as a pivotal factor in the formation of high-temperature superconducting pairings in copper oxides [1], MgB_2 [2] and hydrogen-rich materials under ultrahigh pressure [3].

The search for new superconductors with high transition temperature (T_c) has attracted tremendous interest since the discovery of superconductivity. Inspired by the discovery of high-T_c superconductivity in cuprates and MgB_2, the metallization of σ-bonding electrons has been proposed as a universal guiding principle [4] for discovering high-temperature superconductors. This concept has been widely applied to numerous phonon-mediated superconductors [3, 5–13].

A σ-bond is the strongest covalent bond formed by the direct overlap of two atomic orbitals, each housing a single electron. In contrast, a σ-antibonding state typically corresponds to a repulsive interaction in a diatomic molecule. However, in solid materials, σ-antibonding states can also play a crucial role by contributing to the attractive interaction that binds electrons together, as highlighted in Ref. [14]. Electronic bands originating from hybridized σ-bonding or σ-antibonding orbitals are often situated far below or above the Fermi level.

As discussed in Refs. [4, 14], there are a number of ways to metalize σ-hybrized electrons. One way of inducing metallization involves the application of external pressure, as demonstrated in the hydrogen-rich high-T_c superconductor, SH_3, under ultra-high pressure [3]. This external pressure, combined with the chemical forces exerted on hydrogen atoms by neighbouring atoms, can stabilize crystal structures. It can also alter the electron filling factor, raising the Fermi level crossing the bands formed by the antibonding-σ electrons. An alternative approach is through the exploitation of the crystal field effect, as exemplified by magnesium diboride MgB_2 [4, 5, 15, 16]. In MgB_2, the crystal structure consists of alternating layers of magnesium atoms arranged in a triangular lattice and boron atoms in a honeycomb lattice. The crystal field effect induces a strong attraction between the Mg^{2+} ions and the π electrons in the boron layers, lowering the energy of the bands associated with the hybridized π orbitals. This interaction elevates the energy of the σ-hybridized boron orbitals, bringing them into intersection with the Fermi level. A more general and straightforward strategy is to manipulate the Fermi level by doping. Copper-oxide high-T_c superconductors are typical examples of this type.

The superconductivity in magnesium diboride MgB_2 has spurred interest in exploring other

ARTICLE IN PRESS

superconductors that exhibit metallic σ-bonding electrons [6, 17–26]. Lithium borocarbide LiBC, isoelectronic with MgB_2, has garnered significant attention in this context [17, 18]. While pure LiBC is a band insulator [27, 28], theoretical studies suggest that introducing lithium deficiencies to create hole doping in $Li_{1-x}BC$ could lead to superconductivity at relatively high critical temperatures [17, 18]. However, experimental attempts to synthesize $Li_{1-x}BC$ with finite lithium deficiencies have not been successful in stabilizing the expected crystal structure [27, 29–34], prohibiting the expected metallization of the σ-bonding electrons [34].

To mitigate the lattice instability caused by Li deficiencies, Gao *et al.* suggested partially substituting C atoms with B atoms in LiBC [4, 6]. Through first-principles calculations, they identified two potential superconducting compounds within the $Li_nB_{n+1}C_{n-1}$ series, Li_2B_3C ($n = 2$) and $Li_3B_4C_2$ ($n = 3$), which were predicted to exhibit critical transition temperatures exceeding 50 K. Later on, similar proposals were made by several other groups [19–21].

However, determining the optimal configuration of boron and carbon atoms in $Li_nB_{n+1}C_{n-1}$, known as "the coloring problem" [35, 36], remains a challenge. Gao *et al.* [6] and Bazhirov *et al.* [20] investigated the electronic properties of these compounds using hypothetical crystal structures. Other studies [19, 21] model the substitution effect by employing the virtual crystal approximation.

In this work, we employ the cluster expansion method in conjunction with density functional theory (DFT) to identify energetically stable configurations, also known as optimal colorings, of Li_2B_3C and $Li_3B_4C_2$ [37–39]. Notably, these derived structures deviate significantly from previously proposed configurations with same chemical stoichiometries [6], resulting in totally different electron-phonon coupling (EPC) properties compared with the previous ones. With using the Wannier interpolation technique [40–42], we calculate the EPC properties and find that T_c of Li_2B_3C is unexpectedly low, less than 0.03 K. However, when compressive uniaxial strain (-5%) is applied, the electronic structure of Li_2B_3C is significantly modified, dramatically increasing T_c by over four orders of magnitude to approximately 37 K. This remarkable result provides valuable insights into the complex interplay between electronic structure and phonon-mediated superconductivity. For clarity, we denote the previously proposed $Li_2B_3C/Li_3B_4C_2$ structures from Gao, Lu, and Xiang's work [6] as $Li_2B_3C/Li_3B_4C_2$ (Gao *et al.*), while the configurations proposed in our work are denoted as $Li_2B_3C/Li_3B_4C_2$ (ours).

ARTICLE IN PRESS

II. RESULTS AND DISCUSSION

A. Optimal coloring of $Li_nB_{n+1}C_{n-1}$ (n=2, 3)

To explore the optimal configuration, or "the coloring problem", of B and C atoms within $B_{n+1}C_{n-1}$ layer, we begin with LiBC, whose lattice structure has been well established experimentally. As depicted in our supplementary information (Fig. S3(b)), the B and C atoms in LiBC form an ordered pattern, alternating at the vertices of a hexagonal lattice within each BC layer. However, when B atoms partially replace C atoms, the arrangement of B and C atoms within each $B_{n+1}C_{n-1}$ layer becomes more complex. This "coloring problem" has been largely overlooked in previous studies on $Li_nB_{n+1}C_{n-1}$ [6, 19–21]. For instance, earlier investigations on Li_2B_3C ($n = 2$) and $Li_3B_4C_2$ ($n = 3$) were based on the assumed colorings [6].

To address this issue, we investigated the stable configurations of Li_2B_3C and $Li_3B_4C_2$ using the Cluster Expansion method. Our results (Figs. 1(a-b)) reveal that these colorings are markedly more stable than previously reported configurations with comparable stoichiometries and lattice structures [4], as detailed in Table I. Precisely, in the most stable configurations, B and C atoms are not uniformly distributed within each $B_{n+1}C_{n-1}$ layer. Instead, as marked by green and dark blue frames in Figs. 1(a-b), our $B_{n+1}C_{n-1}$ layers can be visualized as assemblies of alternating B-B and B-C zigzag chains. Moreover, these zigzag chains are interconnected by what we term "bridge bonds" in this study, marked by red and light blue frames in the same figures. Compared with earlier work, these unique arrangements significantly differentiate the colorings in terms of their electronic and electron-phonon coupling properties.

The crystal structures of previously predicted Li_2B_3C (Gao *et al.*) and $Li_3B_4C_2$ (Gao *et al.*) [6] are shown in Figs. 1(c-d). These structures represent two principal variations within the $Li_nB_{n+1}C_{n-1}$ series. The first contains distinct layers of pure B atoms, mixed BC layers, and intervening Li atoms, as exemplified by Li_2B_3C (Gao *et al.*) in Fig. 1(c). Namely, Li_2B_3C (Gao *et al.*) can be construed as a LiBC derivative where half of the B layers are replaced by mixed BC layers. However, the elongated B-B bonds compared to B-C bonds introduce additional energy penalty, as Li_2B_3C (Gao *et al.*) must invest more energy to compress the pure boron layers and expand the boron-carbon layers.

Another principle variation of $Li_nB_{n+1}C_{n-1}$ involves uniform substitution of C atoms by B atoms in each $B_{n+1}C_{n-1}$ layer, such as $Li_3B_4C_2$ (Gao *et al.*) or our low-energy structures. In $Li_3B_4C_2$ (Gao

ARTICLE IN PRESS

et al.), a striking characteristic different from our optimized colorings is the absence of infinitely linked B-B zigzag chains, as illustrated in Fig. 1(d). Instead, the B-B bonds in $Li_3B_4C_2$ (Gao *et al.*) are confined to form isolated triangles that do not interconnect (highlighted as green triangles in Fig. 1(d)).

B. Electronic structures

We calculated the electronic band structures of $Li_nB_{n+1}C_{n-1}$ ($n = 2$ and 3) with DFT method, as illustrated in Fig. 2. The results indicate a clear correlation between the electronic structures and the specific atomic arrangements of these materials. Based on chemical principles, the low-energy bands near the Fermi level are predominantly derived from the sp^2 σ- and p_z π-bonding states of the B and C atoms. Hence, our Wannierization employs the p_z-like Wannier functions (WFs) centered on B or C atoms and s-like bonding WFs centered on the B-B or B-C bond centers.

Owing to the similar lattice structures and chemical stoichiometries, the band structures of $Li_nB_{n+1}C_{n-1}$ share some common features. First, all σ-bonding bands exhibit a highly two-dimensional behavior, as a result of their MgB_2-like lattice. Besides, due to carbon's lower electronegativity compared to boron, the B-C σ-bonding bands lie at a lower energy level than their B-B counterparts. Consequently, as illustrated in Fig. 2, only the π and B-B σ-bonding bands intersect the Fermi level in all $Li_nB_{n+1}C_{n-1}$.

Then let us firstly revisit Li_2B_3C (Gao *et al.*) for comparison. In Li_2B_3C (Gao *et al.*), the B-B σ-bonding WFs and π orbitals dominate the electronic physics near the Fermi level. This renders Li_2B_3C (Gao *et al.*) as an alternative version of MgB_2, albeit with increased hole doping: without considering self-doping from π bands, one hole is doped in one B-B layer (three B-B σ-bonding WFs), so B-B σ-bonding WFs are nearly 5/6-filled.

In $Li_3B_4C_2$ (Gao *et al.*), three 120° rotationally equivalent B-B σ-bonding WFs strongly hybridize with six B-C σ-bonding WFs, as illustrated in Fig. 1(d). As a result, both the B-B and B-C σ-bonding bands in $Li_3B_4C_2$ (Gao *et al.*) exhibit significant hybridization and intersect the Fermi level, influenced by the crystal field effects and boron substitution, as illustrated in Fig. 2(d). While it is established that one hole is doped into the nine σ-bonding bands of the $B_4C_2^{3-}$ layer (without considering self-doping from π bands), the strong hybridization complicates the precise determination of the exact doping level.

However, compared with earlier work, an unique characteristic emerges in the electronic struc-

ARTICLE IN PRESS

tures of our optimal coloring configurations, as a result of their unique structural characteristics. As shown in Figs. 1(a-b) and detailed in Table S2, the B-B bridge bonds are shorter than those within the zigzag chains. This results in larger energy splitting between the bonding and antibonding orbitals across the bridge bonds, leading to lower on-site energies of the B-B σ-bonding WFs in the bridge bonds than those in the zigzag chains. Consequently, the B-B σ-bonding bands from the bridge bonds (along with B-C σ-bonding bands) are fully occupied, while the B-B σ-bonding bands from the zigzag chains, in addition to the π bands, intersect the Fermi level, as depicted in Figs. 2(a-b). Both compounds exhibit comparable doping levels, with approximately 1/2 hole per σ-bonding WF from the B-B zigzag chains (setting aside self-doping from π bands). This similarity is not coincidental; the structural characteristics of these compounds ensure that all bridging σ-bonding WFs are fully occupied, thereby minimizing the electronic energy. We believe that this phenomenon might be a general feature across other $Li_nB_{n+1}C_{n-1}$ compounds.

The electronic structures of $B_{n+1}C_{n-1}$ layers can be quantitatively described using WFs within the tight-binding (TB) approximation. Here we take Li_2B_3C (ours) and $Li_3B_4C_2$ (Gao *et al.*) as two typical examples. The TB Hamiltonian can be written as:

$$H_{TB} = \sum_{\boldsymbol{k}\alpha} \varepsilon_\alpha C^\dagger_{\boldsymbol{k}\alpha} C_{\boldsymbol{k}\alpha} + \sum_{\boldsymbol{k},\alpha\neq\beta} e^{i\boldsymbol{k}R_{\alpha\beta}} t_{\alpha\beta} C^\dagger_{\boldsymbol{k}\alpha} C_{\boldsymbol{k}\beta}, \tag{1}$$

where α/β denotes the index of WFs, ε_α denotes the on-site energy and $t_{\alpha\beta}$ denotes the hopping parameter. Some important TB parameters, on-site energies and nearest-neighbouring hopping parameters of σ-bonding WFs, are detailed in section V of our SI. In these $B_{n+1}C_{n-1}$ layers, the on-site energies of B-B σ-bonding WFs are approximately 1.8 to 2.9 eV higher than those of B-C σ-bonding WFs, so B-C σ-bonding bands are always totally filled. Notably, in Li_2B_3C (ours), the on-site energy of W4, which corresponds to the bridge B-B bond, is 0.5 eV lower than that of the zigzag chain WFs (W2/W3), leading to different doping levels across different kinds of B-B σ-bonding WFs. Conversely, the nearest-neighbouring hopping parameters exhibit similar magnitudes regardless of whether the atomic configurations are optimized, suggesting that variations in hopping strengths do not significantly influence the electronic structures.

C. Electron-phonon coupling

We compute the electron-phonon coupling properties and the resulting superconducting transition temperature for Li_2B_3C and $Li_3B_4C_2$ using the Wannier interpolation technique [40–42].

ARTICLE IN PRESS

To provide a more detailed analysis, we focus on two specific cases: Li_2B_3C (ours) and $Li_3B_4C_2$ (Gao *et al.*). We select Li_2B_3C (ours) due to its orthogonal unit cell containing fewer atoms, which simplifies the electron-phonon coupling calculations and facilitates external strain application in subsequent studies.

We still begin by revisiting $Li_3B_4C_2$ (Gao *et al.*). Our findings for this compound are consistent with those reported in Ref. [6]. As depicted in Fig. 3(d), the twofold degenerate bond-stretching modes, labeled as E', along the Γ-A line exhibit a strong electron-phonon coupling (EPC). The corresponding coupling constant λ and critical temperature T_c are listed in Table II. Our values are slightly lower than those in Ref. [6], where $\lambda = 1.114$ and $T_c \approx 55$ K. This minor deviation is attributed to the larger Gaussian smearing parameter of 0.05 Ry used in our calculations. When we reduce the smearing to 0.02 Ry, matching the value used in Ref. [6], our results closely align, yielding $\lambda = 1.135$ and $T_c = 58.34$ K.

However, as shown in Fig. 3(a), the EPC and the corresponding Eliashberg spectral function for the optimally colored Li_2B_3C are significantly weaker compared to those for $Li_3B_4C_2$ (Gao *et al.*). According to the McMillan-Allen-Dynes formula [43, 44], the superconducting transition temperature T_c is determined by both the logarithmic average phonon frequency ($\omega_{\log}$) and the total EPC strength (λ) in phonon-mediated superconductors. As listed in Table II, the $\omega_{\log}$ of Li_2B_3C (ours) (58.19 meV) is comparable to that of $Li_3B_4C_2$ (Gao *et al.*) (59.54 meV), but the λ value is much lower. This results in an unexpectedly low T_c of approximately 0.03 K for Li_2B_3C (ours), as shown in Fig. 3(b). Similarly, the T_c of $Li_3B_4C_2$ (ours) is also considerably lower than that of $Li_3B_4C_2$ (Gao *et al.*).

Li_2B_3C (ours) and $Li_3B_4C_2$ (Gao *et al.*) also exhibit notable differences in their Fermi surface structures, as shown in Figs. 3(c) and 3(f). For both compounds, the Fermi surfaces corresponding to the σ-bonding bands are relatively flat along the k_z direction due to the weak interlayer coupling of the σ-bonding WFs. However, the σ-bonding Fermi surfaces of Li_2B_3C (ours) are strongly 2D-anisotropic, compared to those of $Li_3B_4C_2$ (Gao *et al.*). This is consistent with the greater dispersion of the σ-bonding bands along the Γ-X direction in Li_2B_3C (ours).

EPC is governed by the deformation potential $D_{\mathbf{q}\nu}$, as described by the equation [5, 9, 45–47]:

$$\lambda_{\mathbf{q}\nu} = N(0)\frac{|D_{\mathbf{q}\nu}|^2}{M_{\mathbf{q}\nu}\omega^2_{\mathbf{q}\nu}}, \tag{2}$$

where $D_{\mathbf{q}\nu}$ denotes the shift in band energy resulting from a perturbation of the phonon mode $\mathbf{q}\nu$ near the Fermi surface, $M_{\mathbf{q}\nu}$ is the averaged atomic mass, and $\omega_{\mathbf{q}\nu}$ is the phonon frequency. The

ARTICLE IN PRESS

strong covalent nature of σ bands results in a large deformation potential, giving a direct physical picture of high critical temperature in MgB_2 [5] or $Li_3B_4C_2$ (Gao *et al.*) [6].

To understand the significant suppression of EPC in the optimal coloring compounds, we examine how the band structures are affected by perturbations in the bond-stretching phonon modes with 0.1 Å amplitude. Fig. 4(b/e) presents the band structures of Li_2B_3C (ours)/$Li_3B_4C_2$ (Gao *et al.*) before and after introducing the perturbation, respectively. For Li_2B_3C (ours), we selected the A_g phonon mode (Fig. 4(a)) as a representative bond-stretching phonon mode due to its strongest electron-phonon coupling (EPC) at the Γ point. For $Li_3B_4C_2$ (Gao *et al.*), we chose the E' mode shown in Fig. 4(d), same as in Ref. [6].

A common observation for both Li_2B_3C (ours) and $Li_3B_4C_2$ (Gao *et al.*) is the significant shift at the top of the σ-bonding bands upon perturbation, as illustrated in Figs. 4(b,e) and highlighted by the dashed purple circles in Figs. 4(c,f). This finding is consistent with previous work on $Li_3B_4C_2$ (Gao *et al.*) [6], where the doubly degenerate σ-bonding bands split by approximately 1.1 eV along the Γ-A direction under the influence of the E' bond-stretching phonon mode, suggesting a strong EPC [6]. This behavior arises because the Fermi level in $Li_3B_4C_2$ (Gao *et al.*) lies near the top of the σ-bonding bands. The top of those σ-bonding bands are strongly coupled with the E' bond-stretching phonon mode and with a large deformation potential.

In contrast, for Li_2B_3C (ours), the top of the σ-bonding bands is either positioned below or well above the Fermi level, indicating that the states at the Fermi level predominantly arise from more dispersive states, which are much less sensitive to lattice vibrations. From a chemist's perspective [48, 49], these dispersive states are primarily contributed by nonbonding electrons. When the perturbation of a bond-stretching phonon mode is introduced, always some bonds are elongated while other bonds are shortened. Consequently, the elongated, weakened bonds lead to smaller energy splitting between the corresponding bonding and antibonding bands while the shortened, strengthened bonds lead to larger energy splitting. For example, in our case, the top of the bridge B-B σ-bonding bands is lifted up while the top of zigzag chain B-B σ-bonding bands is lowered down, because the B-B bonds at the bridge sites are elongated while the B-B bonds in zigzag chains are shortened in the A_g phonon mode, as shown in Figs. 4(a,b). Meanwhile, the dispersive states remain nearly unaffected. Notably, the electronic nature of such scenario is that the Fermi level is positioned near 3/4-filling in Li_2B_3C (ours), as we analyzed in last section. Hence, small deformation potential and weak EPC might be general across other $Li_nB_{n+1}C_{n-1}$ compounds.

The above analysis indicates that achieving a large EPC requires not only the presence of σ-

ARTICLE IN PRESS

bonding character but also a significant deformation potential. Therefore, for the emergence of phonon-mediated high-T_c superconductivity, the states at the Fermi level must exhibit large deformation potentials, which are typically associated with strong covalent bonding or antibonding states. This would help us understand and design new high-temperature superconductors under ambient pressure, such as boron-doped Q-carbon [50] and 2D metal-intercalated borocarbides [51–53].

D. Effect of uniaxial strain

The above analysis suggests that EPC is dramatically suppressed by lattice deformations in the optimal configuration of $Li_nB_{n+1}C_{n-1}$, compared to the $Li_nB_{n+1}C_{n-1}$ (Gao *et al.*) phase. However, since the σ-bonding bands already emerge at the Fermi level, there remains potential to significantly strengthen EPC by tuning the electronic structure to harness the strong covalent bonds in these systems, for instance, through the application of strain. In the cases of both Li_2B_3C (ours) and $Li_3B_4C_2$ (ours), we observe that EPC can be significantly enhanced by applying moderate compressive strain along the b-axis.

Fig. 5(a) illustrates how T_c varies with applied strain for Li_2B_3C (ours), calculated using the McMillan-Allen-Dynes formula [43, 44] with an effective Coulomb potential parameter of $\mu^* = 0.10$. Under -3% b-axis strain, T_c rises to 6.61 K and continues to increase with further strain, forming a dome-like dependence and peaking at 37 K under -5% b-axis strain. Notably, here we use the Gaussian smearing method with the width of 0.05 eV for the Fermi surface broadening in the calculation of EPC. If we choose a smaller smearing width, such as 0.005 eV, T_c can maximally rise to 53 K under -4% b-axis strain.

Similar to the behavior observed in MgB_2 and $Li_3B_4C_2$ (Gao *et al.*), the EPC in Li_2B_3C (ours) is significantly enhanced for bond-stretching phonon modes along the Γ-Z direction when subjected to compressive strain along the b-axis. For example, this enhancement is evident in the changes to both the EPC and electronic structure of Li_2B_3C (ours) under -4% b-axis strain, as shown in Figs. 5(b-c). The dramatic increase in EPC is associated with significant changes in the electronic structure. As illustrated in Figs. 5(c-d), the bridge B-B σ-bonding bands cross the Fermi level, giving rise to elliptical cylindrical Fermi surfaces near the Γ point. Notably, the top of these bridge B-B σ-bonding bands now are above the Fermi level, as highlighted by the dashed purple circles in Fig. 5(c). Compared with the dispersive part, these states are more sensitive to bond-stretching

ARTICLE IN PRESS

vibrations. As a result, this change in electronic structure generates a large deformation potential, leading to a substantial boost in EPC.

The application of compressive strain primarily alters the bond angles and slightly reduces the bond lengths along the b-axis in Li_2B_3C (ours). Concurrently, the lattice constants a and c experience minor elongation. These structural modifications lead to an increase in the hopping parameters from the bridge sites to the zigzag chain sites, while the hopping parameters within the zigzag chains decrease, as detailed in Table S3. For instance, the hopping parameter between W4 and W2 changes from -1.36 eV to -1.46 eV. This adjustment enhances the hybridization between the bridge B-B σ-bonding bands and the zigzag chain B-B σ-bonding bands. Additionally, the compressive strain along the b-axis raises the on-site energies of the σ-bonding WFs at the bridge sites for both B-B and B-C bonds, as detailed in Table S2.

Analyzing Eq. (2), it is important to emphasize the critical role of DOS at the Fermi level in determining EPC [12, 54, 55]. For instance, despite a strong deformation potential, a low DOS can yield weak EPC, as seen in boron-doped diamond [9]. This phenomenon explains why the superconducting transition temperature (T_c) remains low under -3% compressive b-axis strain. Slightly below the -3% compressive b-axis strain, the bridge B-B σ-bonding bands just intersect the Fermi level, triggering a Lifshitz transition. However, such small Fermi surfaces contribute negligibly to DOS at the Fermi level, leading to weak EPC in Li_2B_3C (ours), as shown in Fig. S7(c). As the strain is further increased, more hole are doped in the bridge B-B σ-bonding WFs (Figs. S7(d-f)), enlarging the Fermi surfaces (mainly comprised of bridge B-B σ-bonding WFs) and boosting DOS, even though the deformation potential decreases. The interplay between these two opposing factors results in the characteristic dome-shaped strain-T_c relationship.

III. CONCLUSION

In this paper, we identify the optimal configurations of Li_2B_3C and $Li_3B_4C_2$ using the cluster expansion method, demonstrating that these configurations are thermodynamically more stable than previously reported structures. In these optimized configurations, both B-B and B-C zigzag chains emerge within each $B_{n+1}C_{n-1}$ plane, resulting in unique electronic structures that differ qualitatively from those reported in earlier studies [6, 19–21]. Notably, in $Li_nB_{n+1}C_{n-1}$ (ours) ($n = 2, 3$), only the σ-bonding bands associated with the B-B zigzag chains cross the Fermi level, exhibiting weak hybridization with the σ-bonding bands in the B-C zigzag chains. Additionally,

ARTICLE IN PRESS

the σ-bonding bands in the B-B zigzag chains are approximately 3/4-filled and display significant dispersion along their corresponding directions in reciprocal space. In contrast, other σ-bonding bands remain fully occupied, including the bridge B-B and all B-C σ-bonding bands.

Our calculations of EPC and deformation potential for $Li_3B_4C_2$ (Gao *et al.*) and Li_2B_3C (ours) reveal that both the EPC and deformation potential are significantly weaker in Li_2B_3C (ours) than in $Li_3B_4C_2$ (Gao *et al.*). As a result, the superconducting transition temperature of Li_2B_3C (ours) is less than 0.03 K, dramatically lower than the predicted T_c of 50 K for $Li_3B_4C_2$ (Gao *et al.*). Nonetheless, since the σ-bonding bands in Li_2B_3C (ours) are already present above the Fermi level, there remains significant potential to transform Li_2B_3C (ours) into a phonon-mediated high-T_c superconductor by applying a uniaxial strain. Our strain-dependent calculations show that applying a -5% compressive strain along the b-axis in Li_2B_3C (ours) can markedly alter the electronic band structure around the Fermi level and significantly enhance the deformation potential on the Fermi surface, thereby raising T_c to approximately 37 K. Notably, the deformation potential can be measured by modern experimental techniques nowadays [56–59].

Our work demonstrates that not only the chemical stoichiometry but also the optimal coloring can significantly influence the superconducting pairing interactions. Therefore, it is meaningful to investigate the true coloring of those doped superconductors [50, 60, 61]. Moreover, our findings highlight the critical role of the deformation potential on electrons at the Fermi level, which effectively measures the EPC and is closely linked to the nature of chemical bonding.

ARTICLE IN PRESS

IV. METHODS

In order to build cluster expansion of the energy, we firstly employ VASP [62, 63] to perform DFT calculations for different configurations in certain AlB_2-type supercells with PBEsol functional [64]. The cluster expansions are constructed using the alloy theoretic automated toolkit (ATAT) [65]. To fit ECI with DFT results, we consider different randomly generated configurations in the $2 \times 2 \times 2$ and the $2 \times 3 \times 2$ AlB_2-type supercells with different proportion of boron to carbon. For each configuration, both the lattice constants and internal coordinates are fully relaxed while the energy convergence criterion is 10^{-6} eV and the force convergence criterion is 0.01 eV/Å. The projector augmented wave [66] (PAW) approach is employed and the cut-off energy of the plane wave basis is 600 eV. The Brillouin zones in supercells are sampled by $\mathbf{k}$-grids as dense as a Γ-centered $6 \times 6 \times 6$ $\mathbf{k}$-grid in an AlB_2-type unit cell. LOOCVs of both Li_2B_3C and $Li_3B_4C_2$

ARTICLE IN PRESS

are smaller than 0.01 eV.

We employ Wannier90 [67, 68] interfacing with Quantum ESPRESSO [69] to calculate maximally localized WFs for analyzing electronic structures. We also calculate the lattice constants and total energy with Quantum ESPRESSO. We adopt PBE exchange-correlation functional [70] and the SG15 norm-conserving pseudopotentials [71–73]. The crystal structures are fully relaxed while the energy convergence criterion is 10^{-12} Ry and the force convergence criterion is 10^{-6} Ry/Bohr. The kinetic energy cutoff is set to 80 Ry. The Marzari-Vanderbilt-DeVita-Payne smearing method [74] is employed with the spreading of 0.015 Ry. The **k**-grid is $16 \times 8 \times 6$/$16 \times 16 \times 6$/$12 \times 12 \times 12$/$9 \times 9 \times 12$ for Li_2B_3C (ours)/Li_2B_3C (Gao *et al.*)/$Li_3B_4C_2$ (ours)/$Li_3B_4C_2$ (Gao *et al.*), respectively. The energy windows and frozen windows for the disentanglement procedure in Wannierization are listed in Table S1. The Wannier centers are set on B/C atoms for p_z-like WFs and on B-B/B-C bond center for s-like B-B/B-C bonding WFs.

We employ EPW package [41, 42] to calculate the electron-phonon coupling properties of Li_2B_3C (ours) and $Li_3B_4C_2$ (Gao *et al.*). We take the $16 \times 8 \times 6$/$9 \times 9 \times 12$ **k**-mesh and $8 \times 4 \times 3$/$3 \times 3 \times 4$ **q**-mesh as coarse grids and then interpolate them to the dense $64 \times 32 \times 24$/$36 \times 36 \times 48$ **k**-mesh and $16 \times 8 \times 6$/$9 \times 9 \times 12$ **q**-mesh in Li_2B_3C (ours)/$Li_3B_4C_2$ (Gao *et al.*), respectively. The Gaussian smearing method with the width of 0.05 eV is used for the Fermi surface broadening.

The superconducting transition temperature T_c is calculated with the McMillan-Allen-Dynes fomula [43, 44]:

$$T_c = \frac{\omega_{\log}}{1.2}\exp[\frac{-1.04(1+\lambda)}{\lambda(1-0.62\mu^*)-\mu^*}]. \tag{3}$$

Here λ is the total EPC strength, μ^* is a parameter as the effect screened Coulomb pseudopotential and $\omega_{\log}$ is the logarithmic average of the Eliashberg spectral function. λ and $\omega_{\log}$ are defined as:

$$\lambda = \sum_{\mathbf{q}\nu}\lambda_{\mathbf{q}\nu} = 2\int\frac{\alpha^2F(\omega)}{\omega}\mathrm{d}\omega, \tag{4}$$

$$\omega_{\log} = \exp[\frac{2}{\lambda}\int\frac{\mathrm{d}\omega}{\omega}\alpha^2F(\omega)ln(\omega)], \tag{5}$$

$$\alpha^2F(\omega) = \frac{1}{2}\sum_{\mathbf{q}\nu}\delta(\omega-\omega_{\mathbf{q}\nu})\omega_{\mathbf{q}\nu}\lambda_{\mathbf{q}\nu}. \tag{6}$$

Here $\omega_{\mathbf{q}\nu}$ and $\lambda_{\mathbf{q}\nu}$ are the frequency and EPC strength of the ν-th phonon mode at the wave vector **q**. The $\lambda_{\mathbf{q}\nu}$ is defined as:

$$\lambda_{\mathbf{q}\nu} = \frac{\gamma_{\mathbf{q}\nu}}{\pi\hbar N(0)\omega^2_{\mathbf{q}\nu}}. \tag{7}$$

ARTICLE IN PRESS

Here $\gamma_{\mathbf{q}\nu}$ is the phonon linewidth:

$$\gamma_{\mathbf{q}\nu} = 2\pi\omega_{\mathbf{q}\nu}\sum_{i,j}\int\frac{\mathrm{d}\mathbf{k}}{\Omega_{BZ}}|g_{\mathbf{q}\nu}(\mathbf{k},i,j)|^2\delta(\epsilon_{\mathbf{k},i}-\epsilon_F)\delta(\epsilon_{\mathbf{k}+\mathbf{q},j}-\epsilon_F). \tag{8}$$

Here i/j is the band index. The electron-phonon interaction matrix element $g_{\mathbf{q}\nu}(\mathbf{k},i,j)$, describing the probability amplitude for scattering of an electron with a transfer of crystal momentum $\mathbf{q}$, is determined by:

$$\begin{aligned} g_{\mathbf{q}\nu}(\mathbf{k},i,j) &= \sqrt{\frac{\hbar}{2\omega_{\mathbf{q}\nu}}} < \psi_{\mathbf{k},i}|\Delta V_{KS}^{\mathbf{q}\nu}|\psi_{\mathbf{k}+\mathbf{q},j} >; \\ \Delta V_{KS}^{\mathbf{q}\nu} &= \sum_{\mathbf{R},s}\frac{\partial V_{KS}}{\partial \mathbf{u}_{s\mathbf{R}}}\mathbf{u}_s^{\mathbf{q}\nu}\frac{e^{i\mathbf{q}\mathbf{R}}}{\sqrt{N}} \end{aligned} \tag{9}$$

Here $\mathbf{u}_s^{\mathbf{q}\nu} = \frac{\nu_s^{\mathbf{q}\nu}}{\sqrt{M_s}}$ and $\frac{\partial V_{KS}}{\partial \mathbf{u}_{s\mathbf{R}}}$ can be calculated by density functional perturbation theory (DFPT) [75].

ARTICLE IN PRESS

ARTICLE IN PRESS

Acknowledgement

We thank Xi Xu and Yue-chao Wang for useful discussions. The work is supported by the National Natural Science Foundation of China (Grant No: 22273002, 12404153) and the Fundamental Research Fund for the Central Universities (Grant No: FRF-TP-25-040). The calculations were done on Hefei advanced computing center, etc.

Author Contributions

Jiangping Hu, Hong Jiang and Yuhao Gu designed the project. Yuhao Gu performed the first-principles calculations. Yuhao Gu, Tao Xiang and Hong Jiang wrote the manuscript. All authors participated in discussions and provided comments on the manuscript.

Competing interests

The authors declare no competing interests.

Data availability

The data that support the findings of this study are available from the corresponding author upon reasonable request.

Code availability

The calculations were performed using the proprietary code VASP [62], the open-source code ATAT [65], the open-source code Wannier90 [67], the open-source code Quantum ESPRESSO [69], and the open-source code EPW [42]. Wannier90 and EPW are freely released under the GNU General Public License (v2). ATAT and Quantum ESPRESSO are freely released under the Creative Commons Attribution 4.0 International License.

ARTICLE IN PRESS

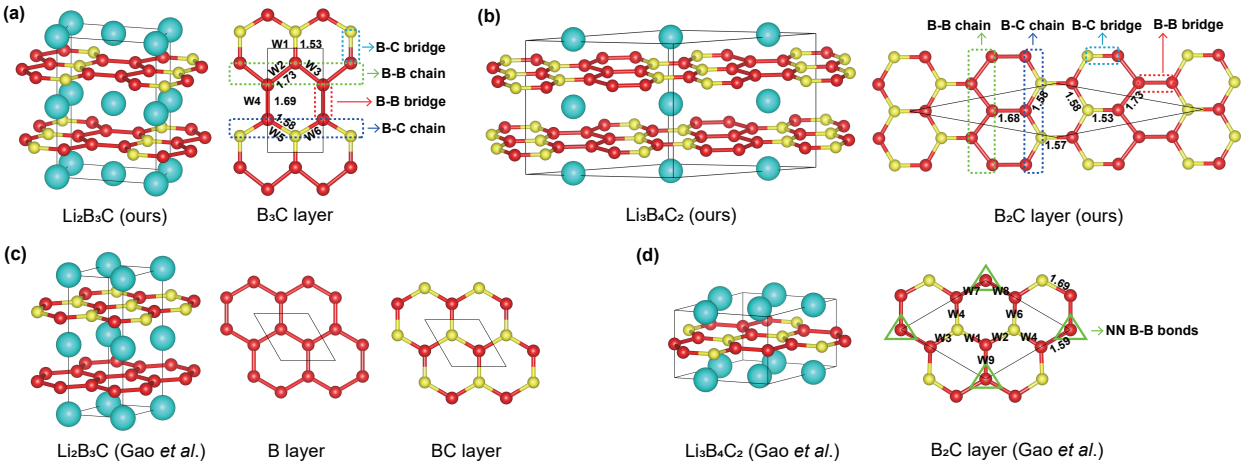

FIG. 1. Crystal structures of $Li_nB_{n+1}C_{n-1}$: (a-b) Li_2B_3C and $Li_3B_4C_2$ with optimal configurations from this work (ours), (c-d) Li_2B_3C and $Li_3B_4C_2$ proposed by Gao, Lu, and Xiang (Gao *et al.*) [6]. In (a-b), B-C bridge bonds, B-B zigzag chains, B-B bridge bonds and B-C zigzag chains are marked by light blue, green, red and dark blue frames, respectively. Green triangles in (d) indicate three nearest-neighbouring B-B bonds. The lengths of bonds are labeled in figure and the unit is angstrom. Atom color key: light blue (Li), red (B), yellow (C).

ARTICLE IN PRESS

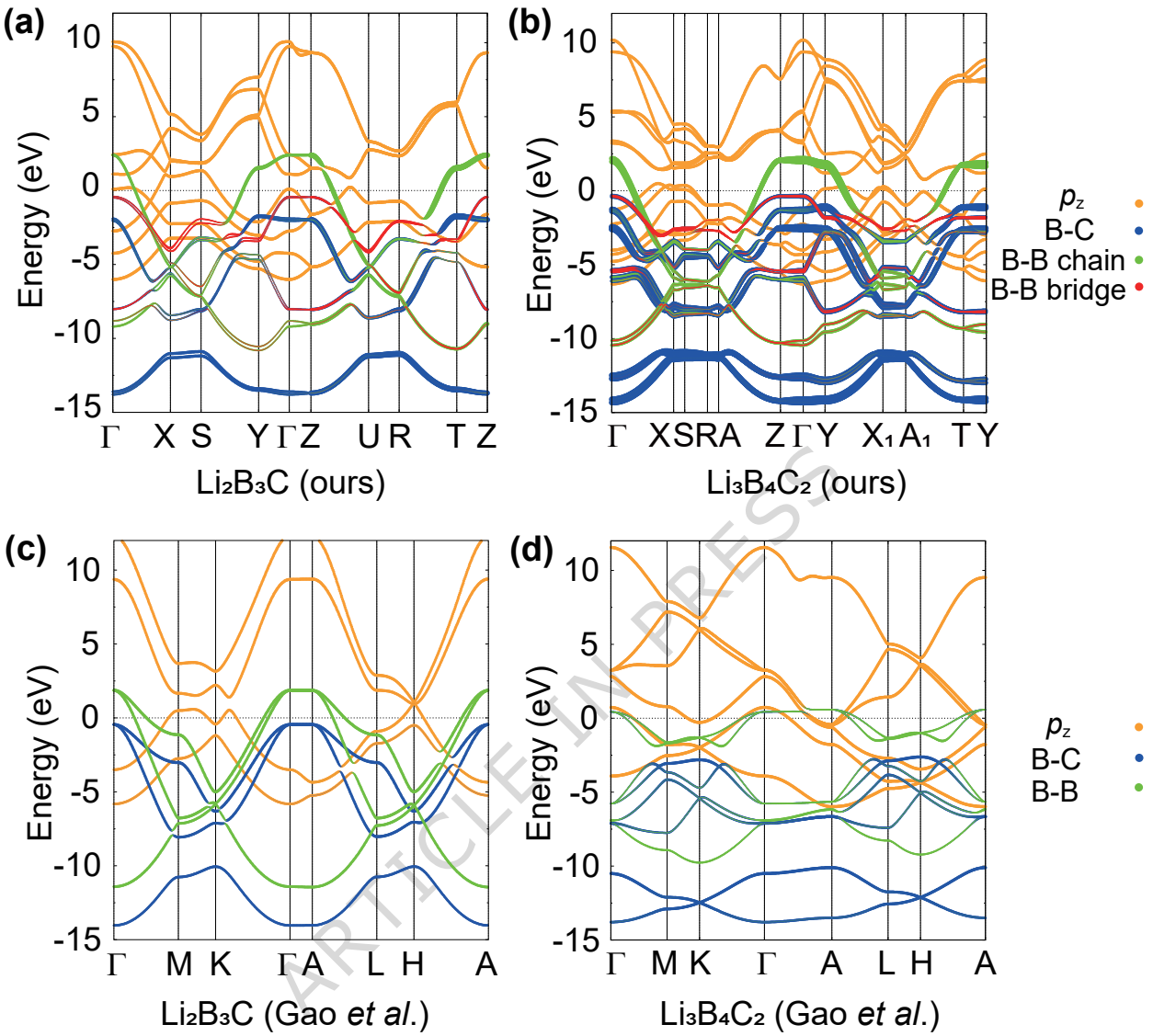

FIG. 2. Band structures for (a) Li_2B_3C (ours), (b) $Li_3B_4C_2$ (ours), (c) Li_2B_3C (Gao *et al.*), and (d) $Li_3B_4C_2$ (Gao *et al.*). The dot sizes are proportional to the spectral weights obtained from Wannierization. The high-symmetry **k**-points are detailed in Fig. S2 of our SI.

ARTICLE IN PRESS

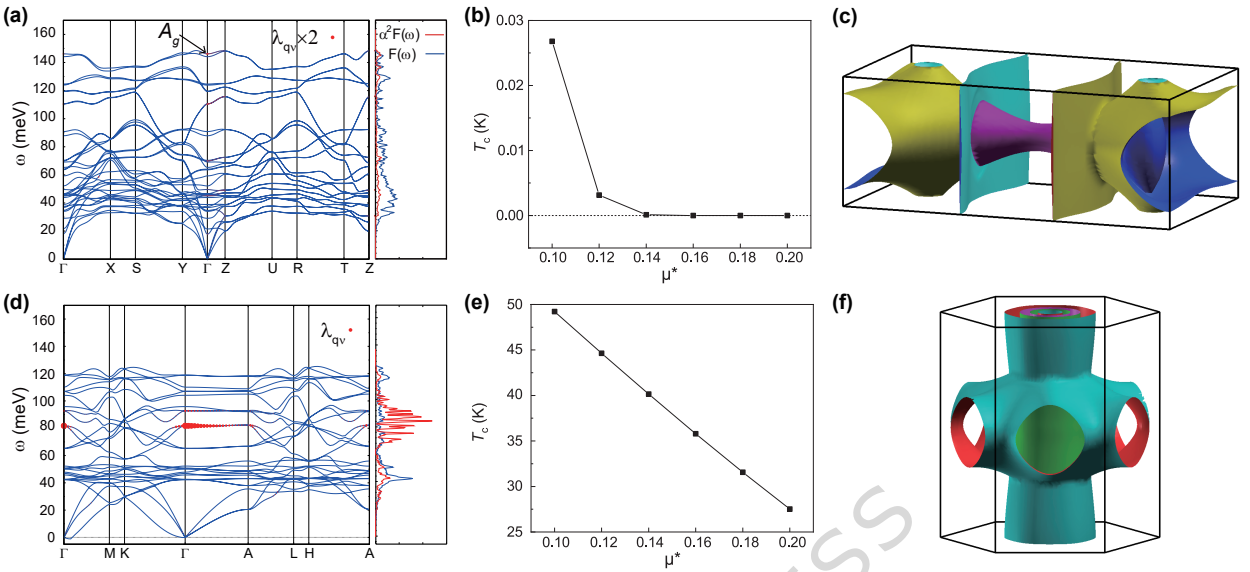

FIG. 3. Electron-phonon coupling constant $\lambda_{\mathbf{q}\nu}$ and Fermi surface contours for (a-c) Li_2B_3C (ours) and (d-f) $Li_3B_4C_2$ (Gao *et al.*). Panels (a) and (d) show the phonon band dispersions along with the corresponding EPC strengths $\lambda_{\mathbf{q}\nu}$, where the size of the red dots indicates the magnitude of $\lambda_{\mathbf{q}\nu}$. The sizes of dots are doubled in (a) for aesthetic visualization. The right subpanels display the phonon density of states (blue curves) and the Eliashberg spectral functions (red curves). Panels (b) and (e) illustrate the variation of the superconducting transition temperature T_c as a function of the Coulomb pseudopotential parameter μ^*. Panels (c) and (f) depict the Fermi surfaces for each compound.

ARTICLE IN PRESS

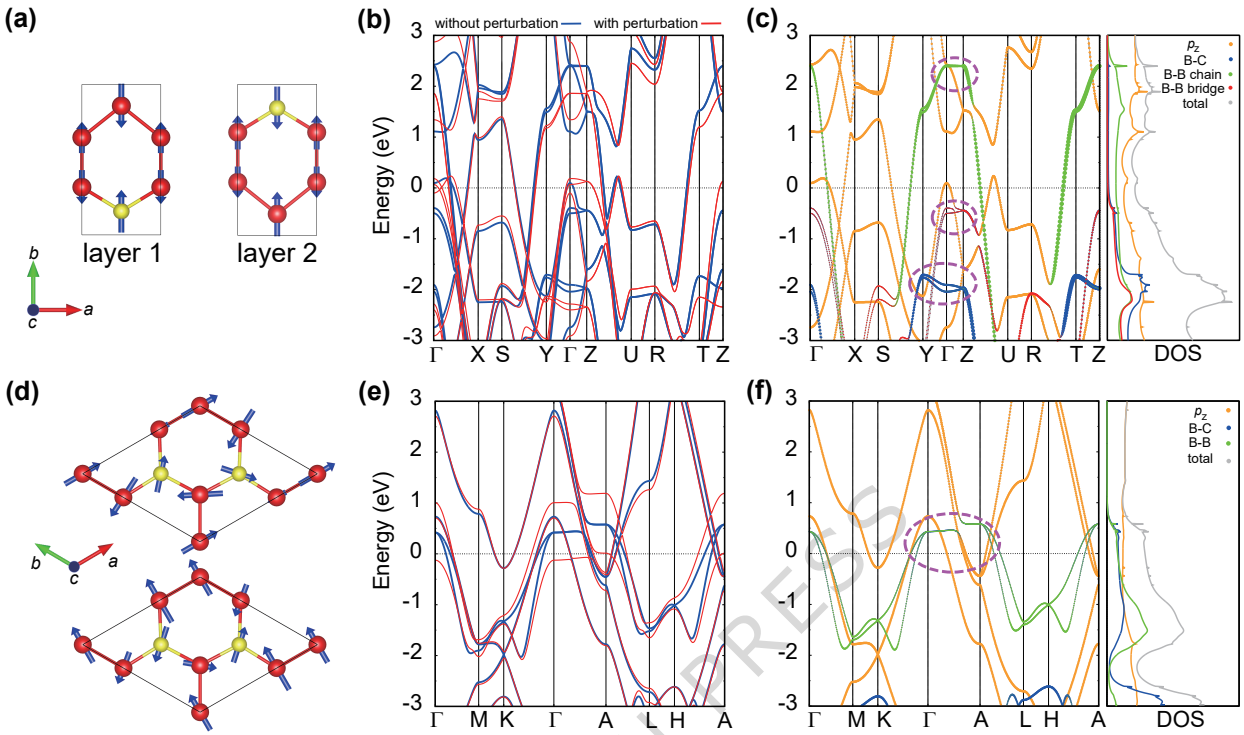

FIG. 4. Effects of atomic displacements associated with specific bond-stretching phonon vibration modes on the electronic band structures for Li_2B_3C (ours) and $Li_3B_4C_2$ (Gao *et al.*). (a) Illustration of the A_g phonon mode at the Γ point for Li_2B_3C (ours), occurring at approximately 140 meV. Blue arrows indicate the directions of atomic displacements, while their lengths represent the relative amplitudes of the phonon mode. (b) Electronic band structure of Li_2B_3C (ours) with a perturbation from an amplitude of 0.1 Å corresponding to the A_g phonon mode (red curve) compared to the band structure of the fully relaxed crystal structure (blue curve). (c) Projected band structure and density of states (DOS) of Li_2B_3C (ours), highlighting the top of the σ-bonding bands near the Γ point, which are sensitive to phonon vibrations, marked by dashed purple circles. (d) Illustration of the E' phonon mode at the Γ point for $Li_3B_4C_2$ (Gao *et al.*), occurring near 80 meV. Blue arrows indicate the directions of atomic displacements, while their lengths represent the relative amplitudes of the phonon mode. (e) Electronic band structure of $Li_3B_4C_2$ (Gao *et al.*) with a perturbation from an amplitude of 0.1 Å corresponding to the E' phonon mode (red curve) compared to the band structure of the fully relaxed crystal structure (blue curve). (f) Projected band structure and DOS of $Li_3B_4C_2$ (Gao *et al.*), highlighting the top of the σ-bonding bands near the Γ point, which are sensitive to phonon vibrations, marked by dashed purple circles.

ARTICLE IN PRESS

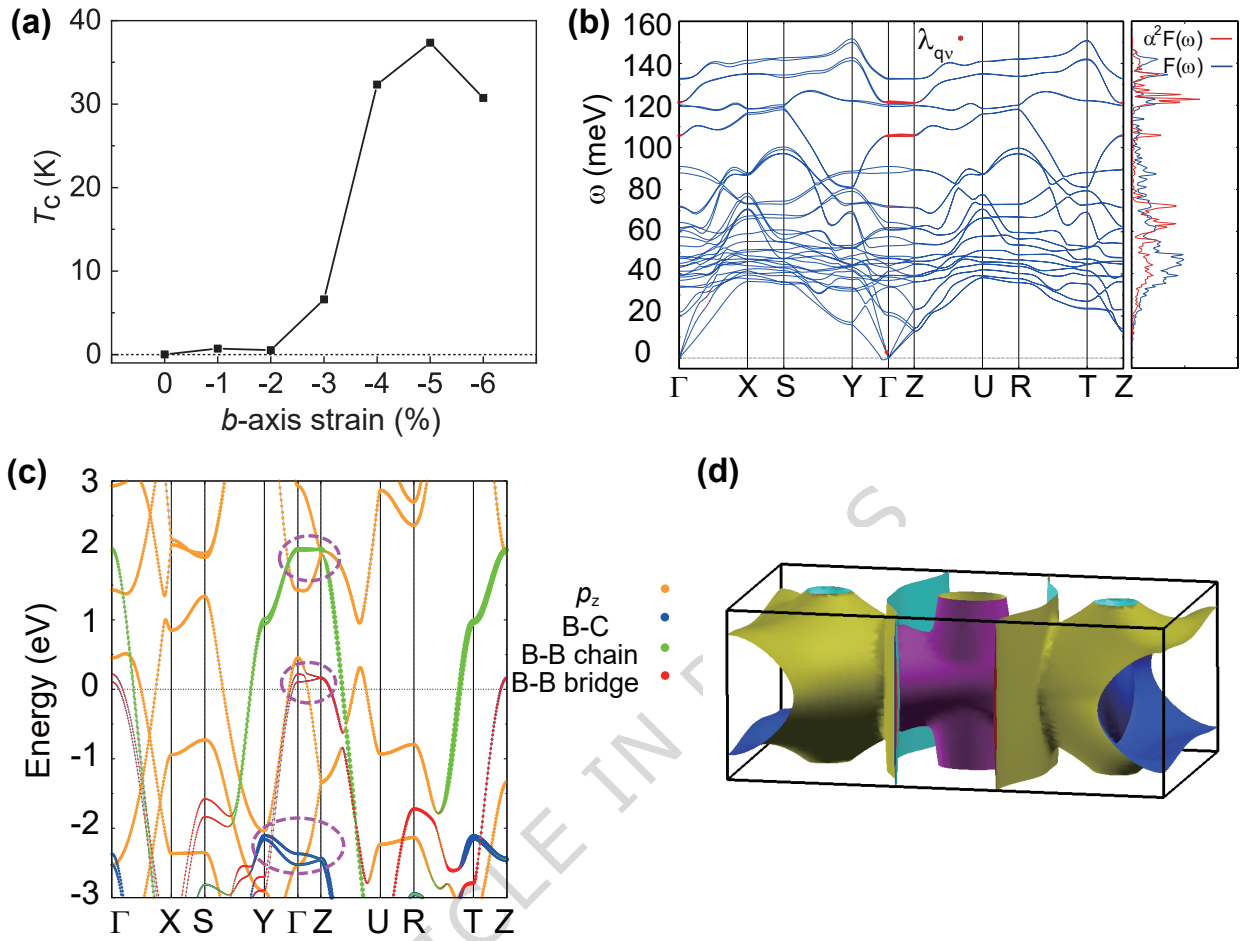

FIG. 5. Impact of compressive b-axis strain on the superconducting transition temperature and electronic structure of Li_2B_3C (ours). (a) T_c as a function of compressive b-axis strain with $\mu^* = 0.10$. (b) Phonon dispersion under -4% compressive b-axis strain, where the red dot size is proportional to the electron-phonon coupling strength, $\lambda_{\mathbf{q}\nu}$. The right panel displays the phonon density of states (blue line) and the Eliashberg spectral function (red line). (c) Projected band structure under -4% compressive b-axis strain, with dot sizes representing the spectral weights. The top of the σ-bonding bands near the Γ point, sensitive to phonon vibrations, are indicated by dashed purple circles. (d) Fermi surfaces under -4% compressive b-axis strain.

ARTICLE IN PRESS

TABLE I. The energies, space groups and lattice parameters for Li_2B_3C (ours/Gao *et al.*) and $Li_3B_4C_2$ (ours/Gao *et al.*) after structural relaxation. The ground state energy for each formula is set as 0. Note that the lattice parameters here are for conventional cells while we use the primitive cell of $Li_3B_4C_2$ (ours) in our calculations.

System	Energy per formula (eV)	Space group	a (Å)	b (Å)	c (Å)
Li_2B_3C (ours)	0	$Pmma$	2.71	5.11	7.21
Li_2B_3C (Gao *et al.*)	0.327	$P\bar{6}m2$	2.84	2.84	7.13
$Li_3B_4C_2$ (ours)	0	$Cmcm$	14.93	2.73	7.17
$Li_3B_4C_2$ (Gao *et al.*)	0.354	$P\bar{6}m2$	4.88	4.88	3.52

TABLE II. The calculated superconducting parameters for Li_2B_3C (ours) and $Li_3B_4C_2$ (Gao *et al.*). The μ^* here is 0.10.

Compound	$\omega_{\log}$ (meV)	λ	T_c (K)
Li_2B_3C (ours)	58.19	0.26	0.03
$Li_3B_4C_2$ (Gao *et al.*)	59.54	0.96	49.22

ARTICLE IN PRESS

ARTICLE IN PRESS

References

[1] Bednorz, J. G. & Müller, K. A. Possible high T_c superconductivity in the Ba-La-Cu-O system. *Zeitschrift für Physik B Condensed Matter* **64**, 189–193 (1986).

[2] Nagamatsu, J., Nakagawa, N., Muranaka, T., Zenitani, Y. & Akimitsu, J. Superconductivity at 39 K in magnesium diboride. *Nature* **410**, 63–64 (2001).

[3] Drozdov, A., Eremets, M., Troyan, I., Ksenofontov, V. & Shylin, S. I. Conventional superconductivity at 203 Kelvin at high pressures in the sulfur hydride system. *Nature* **525**, 73–76 (2015).

[4] Gao, M., Lu, Z.-Y. & Xiang, T. Finding high-temperature superconductors by metallizing the σ-bonding electrons. *PHYSICS (in Chinese)* **44**, 421–426 (2015).

[5] An, J. M. & Pickett, W. E. Superconductivity of MgB_2: Covalent Bonds Driven Metallic. *Phys. Rev. Lett.* **86**, 4366–4369 (2001).

[6] Gao, M., Lu, Z.-Y. & Xiang, T. Prediction of phonon-mediated high-temperature superconductivity in $Li_3B_4C_2$. *Phys. Rev. B* **91**, 045132 (2015).

[7] Deng, S., Simon, A. & Köhler, J. Superconductivity in MgB_2: A case study of the "flat Band–Steep band" scenario. *J. Supercond.* **16**, 477–481 (2003).

[8] Deng, S., Simon, A. & Köhler, J. A" flat/steep band" model for superconductivity. *Inter. J. Mod. Phys. B* **19**, 29–36 (2005).

[9] Lee, K.-W. & Pickett, W. E. Superconductivity in boron-doped diamond. *Phys. Rev. Lett.* **93**, 237003 (2004).

[10] Peng, F. *et al.* Hydrogen clathrate structures in rare earth hydrides at high pressures: possible route to room-temperature superconductivity. *Phys. Rev. Lett.* **119**, 107001 (2017).

[11] Gu, Y., Wu, X., Jiang, K. & Hu, J. $BaCuS_2$: a superconductor with moderate electron-electron correlation. *Chin. Phys. Lett.* **38**, 017501 (2021).

[12] Geng, N. *et al.* Conventional high-temperature superconductivity in metallic, covalently bonded, binary-guest c–b clathrates. *J. Am. Chem. Soc.* **145**, 1696–1706 (2023).

[13] Geng, N., Hilleke, K. P., Belli, F., Das, P. K. & Zurek, E. Superconductivity in CH_4 and BH_4-containing compounds derived from the high-pressure superhydrides. *Mater. Today Phys.* **44**, 101443 (2024).

ARTICLE IN PRESS

[14] Zhang, J.-F. *et al.* Vital influence of hydrogen σ antibonding states on high-T_c superconductivity in SH_3 under ultrahigh pressure. *Phys. Rev. B* **108**, 094519 (2023).

[15] Kortus, J., Mazin, I. I., Belashchenko, K. D., Antropov, V. P. & Boyer, L. L. Superconductivity of metallic boron in MgB_2. *Phys. Rev. Lett.* **86**, 4656–4659 (2001).

[16] Xi, X. X. Two-band superconductor magnesium diboride. *Rep. Prog. Phys.* **71**, 116501 (2008).

[17] Rosner, H., Kitaigorodsky, A. & Pickett, W. Prediction of high T_c superconductivity in hole-doped LiBC. *Phys. Rev. Lett.* **88**, 127001 (2002).

[18] Dewhurst, J., Sharma, S., Ambrosch-Draxl, C. & Johansson, B. First-principles calculation of superconductivity in hole-doped LiBC: $T_c = 65K$. *Phys. Rev. B* **68**, 020504 (2003).

[19] Miao, R. *et al.* First-principles study of superconductivity in the hole self-doped $LiB_{1.1}C_{0.9}$. *J. Appl. Phys.* **113**, 133910 (2013).

[20] Bazhirov, T., Sakai, Y., Saito, S. & Cohen, M. L. Electron-phonon coupling and superconductivity in Li -intercalated layered borocarbide compounds. *Phys. Rev. B* **89**, 045136 (2014).

[21] Li, Q.-Z., Yan, X.-W., Gao, M. & Wang, J. Electron-phonon coupling and superconductivity in $LiB_{1+x}C_{1-x}$. *Euro. Phys. Lett.* **122**, 47001 (2018).

[22] Quan, Y. & Pickett, W. E. $Li_{2x}BC_3$: Prediction of a second MgB_2-class high-temperature superconductor. *Phys. Rev. B* **102**, 144504 (2020).

[23] Liu, H.-D., Wang, B.-T., Fu, Z.-G., Lu, H.-Y. & Zhang, P. Three-gap superconductivity with T_c above 80 K in hydrogenated 2D monolayer LiBC. *Phys. Rev. Res.* **6**, 033241 (2024).

[24] Yu, W. *et al.* Nontrivial d-electrons driven superconductivity of transition metal diborides. *New J. Phys.* (2024).

[25] Pickett, W. E. Design for a room-temperature superconductor. *J. Supercond. Nov. Mag.* **19**, 291–297 (2006).

[26] Pickett, W. E. Room temperature superconductivity revolution: Foreshadowed by victorians, enabled by millenials. *arXiv preprint arXiv:1801.00165* (2017).

[27] Fogg, A., Chalker, P., Claridge, J., Darling, G. & Rosseinsky, M. LiBC electronic, vibrational, structural, and low-temperature chemical behavior of a layered material isoelectronic with MgB_2. *Phys. Rev. B* **67**, 245106 (2003).

[28] Karimov, P. *et al.* Resonant inelastic soft x-ray scattering and electronic structure of LiBC. *J. Phys. Condens. Matter* **16**, 5137 (2004).

[29] Bharathi, A. *et al.* Synthesis and search for superconductivity in LiBC. *Solid State Commun.* **124**,

ARTICLE IN PRESS

423–428 (2002).

[30] Fogg, A., Claridge, J., Darling, G. & Rosseinsky, M. Synthesis and characteristion of Li_xBC—hole doping does not induce superconductivity. *Chem. Commun.* 1348–1349 (2003).

[31] Souptel, D., Hossain, Z., Behr, G., Löser, W. & Geibel, C. Synthesis and physical properties of LiBC intermetallics. *Solid State Commun.* **125**, 17–21 (2003).

[32] Zhao, L., Klavins, P. & Liu, K. Synthesis and properties of hole-doped $Li_{1-x}BC$. *J. Appl. Phys.* **93**, 8653–8655 (2003).

[33] Nakamori, Y. & Orimo, S.-i. Synthesis and characterization of single phase Li_xBC (x= 0.5 and 1.0), using Li hydride as a starting material. *J. Alloys Compd.* **370**, L7–L9 (2004).

[34] Fogg, A. M., Meldrum, J., Darling, G. R., Claridge, J. B. & Rosseinsky, M. J. Chemical control of electronic structure and superconductivity in layered borides and borocarbides: understanding the absence of superconductivity in Li_xBC. *J. Am. Chem. Soc.* **128**, 10043–10053 (2006).

[35] Burdett, J. K., Lee, S. & McLarnan, T. J. Coloring problem. *J. Am. Chem. Soc.* **107**, 3083–3089 (1985).

[36] Miller, G. J. The "coloring problem" in solids: How it affects structure, composition and properties. *Euro. J. Inorg. Chem.* 523–536 (1998).

[37] Sanchez, J. M., Ducastelle, F. & Gratias, D. Generalized cluster description of multicomponent systems. *Phys. A: Stat. Mech. Appl.* **128**, 334–350 (1984).

[38] De Fontaine, D. Cluster approach to order-disorder transformations in alloys. *Solid State Phys.* **47**, 33–176 (1994).

[39] Zunger, A. *First-principles statistical mechanics of semiconductor alloys and intermetallic compounds*, 361–419 (Springer, 1994).

[40] Giustino, F., Cohen, M. L. & Louie, S. G. Electron-phonon interaction using wannier functions. *Phys. Rev. B* **76**, 165108 (2007).

[41] Poncé, S., Margine, E. R., Verdi, C. & Giustino, F. EPW: Electron–phonon coupling, transport and superconducting properties using maximally localized wannier functions. *Comput. Phys. Commun.* **209**, 116–133 (2016).

[42] Lee, H. *et al.* Electron-phonon physics from first principles using the EPW code. *Npj Comput. Mater.* **9** (2023).

[43] Allen, P. B. Neutron spectroscopy of superconductors. *Phys. Rev. B* **6**, 2577 (1972).

[44] Allen, P. B. & Dynes, R. Transition temperature of strong-coupled superconductors reanalyzed. *Phys.*

ARTICLE IN PRESS

Rev. B **12**, 905 (1975).

[45] Khan, F. & Allen, P. Deformation potentials and electron-phonon scattering: Two new theorems. *Phys. Rev. B* **29**, 3341 (1984).

[46] Lee, K.-W. & Pickett, W. Crystal symmetry, electron-phonon coupling, and superconducting tendencies in Li_2Pd_3B and Li_2Pt_3B. *Phys. Rev. B* **72**, 174505 (2005).

[47] Tan, H., Liu, Y., Wang, Z. & Yan, B. Charge density waves and electronic properties of superconducting kagome metals. *Phys. Rev. Lett.* **127**, 046401 (2021).

[48] Hoffmann, R. *Solids and surfaces: a chemist's view of bonding in extended structures* (John Wiley & Sons, 1991).

[49] Dronskowski, R. & Blöchl, P. E. Crystal orbital hamilton populations (COHP): energy-resolved visualization of chemical bonding in solids based on density-functional calculations. *J. Phys. Chem.* **97**, 8617–8624 (1993).

[50] Bhaumik, A., Sachan, R. & Narayan, J. High-temperature superconductivity in boron-doped Q-carbon. *ACS nano* **11**, 5351–5357 (2017).

[51] Gao, M., Yan, X.-W., Lu, Z.-Y. & Xiang, T. Strong-coupling superconductivity in LiB_2C_2 trilayer films. *Phys. Rev. B* **101**, 094501 (2020).

[52] Zhang, Y., Chen, J., Hao, J., Xu, M. & Li, Y. Conventional high-temperature superconductivity in σ-band driven metallized two-dimensional metal borocarbides. *Phys. Rev. B* **110**, 064513 (2024).

[53] Liu, H.-D., Fu, X.-P., Fu, Z.-G., Lu, H.-Y. & Zhang, P. High-T_c and three-gap two-dimensional superconductors with electronic and phononic topology: KB_2C_2. *Phys. Rev. B* **111**, 184502 (2025).

[54] Sano, W., Koretsune, T., Tadano, T., Akashi, R. & Arita, R. Effect of Van hove singularities on high-T_c superconductivity in H_3S. *Phys. Rev. B* **93**, 094525 (2016).

[55] Gai, T.-T. *et al.* Van hove singularity induced phonon-mediated superconductivity above 77 K in hole-doped SrB_3C_3. *Phys. Rev. B* **105**, 224514 (2022).

[56] Gerber, S. *et al.* Femtosecond electron-phonon lock-in by photoemission and x-ray free-electron laser. *Science* **357**, 71–75 (2017).

[57] Huang, Y. *et al.* Ultrafast Measurements of Mode-Specific Deformation Potentials of Bi_2Te_3 and Bi_2Se_3. *Phys. Rev. X* **13**, 041050 (2023).

[58] Sobota, J. A., He, Y. & Shen, Z.-X. Angle-resolved photoemission studies of quantum materials. *Rev. Mod. Phys.* **93**, 025006 (2021).

[59] Boschini, F., Zonno, M. & Damascelli, A. Time-resolved arpes studies of quantum materials. *Rev.*

ARTICLE IN PRESS

Mod. Phys. **96**, 015003 (2024).

[60] Sun, H. *et al.* Signatures of superconductivity near 80 K in a nickelate under high pressure. *Nature* **621**, 493–498 (2023).

[61] Ding, X. *et al.* Critical role of hydrogen for superconductivity in nickelates. *Nature* **615**, 50–55 (2023).

[62] Kresse, G. & Furthmüller, J. Efficient iterative schemes for ab initio total-energy calculations using a plane-wave basis set. *Phys. Rev. B* **54**, 11169 (1996).

[63] Kresse, G. & Joubert, D. From ultrasoft pseudopotentials to the projector augmented-wave method. *Phys. Rev. B* **59**, 1758 (1999).

[64] Perdew, J. P. *et al.* Restoring the density-gradient expansion for exchange in solids and surfaces. *Phys. Rev. Lett.* **100**, 136406 (2008).

[65] Van De Walle, A., Asta, M. & Ceder, G. The alloy theoretic automated toolkit: A user guide. *Calphad* **26**, 539–553 (2002).

[66] Blöchl, P. E. Projector augmented-wave method. *Phys. Rev. B* **50**, 17953 (1994).

[67] Mostofi, A. A. *et al.* Wannier90: A tool for obtaining maximally-localised Wannier functions. *Comput. Phys. Commun.* **178**, 685–699 (2008).

[68] Marzari, N., Mostofi, A. A., Yates, J. R., Souza, I. & Vanderbilt, D. Maximally localized Wannier functions: Theory and applications. *Rev. Mod. Phys.* 1419–1475 (2012).

[69] Giannozzi, P. *et al.* Quantum espresso: a modular and open-source software project for quantum simulations of materials. *J. Phys. Condens. Matter* **21**, 395502 (2009).

[70] Perdew, J. P., Burke, K. & Ernzerhof, M. Generalized gradient approximation made simple. *Phys. Rev. Lett.* **77**, 3865 (1996).

[71] Troullier, N. & Martins, J. L. Efficient pseudopotentials for plane-wave calculations. *Phys. Rev. B* **43**, 1993 (1991).

[72] Hamann, D. Optimized norm-conserving vanderbilt pseudopotentials. *Phys. Rev. B* **88**, 085117 (2013).

[73] Schlipf, M. & Gygi, F. Optimization algorithm for the generation of ONCV pseudopotentials. *Comput. Phys. Commun.* **196**, 36–44 (2015).

[74] Marzari, N., Vanderbilt, D., De Vita, A. & Payne, M. Thermal contraction and disordering of the Al (110) surface. *Phys. Rev. Lett.* **82**, 3296 (1999).

[75] Baroni, S., De Gironcoli, S., Dal Corso, A. & Giannozzi, P. Phonons and related crystal properties from density-functional perturbation theory. *Rev. Mod. Phys.* **73**, 515 (2001).

ARTICLE IN PRESS

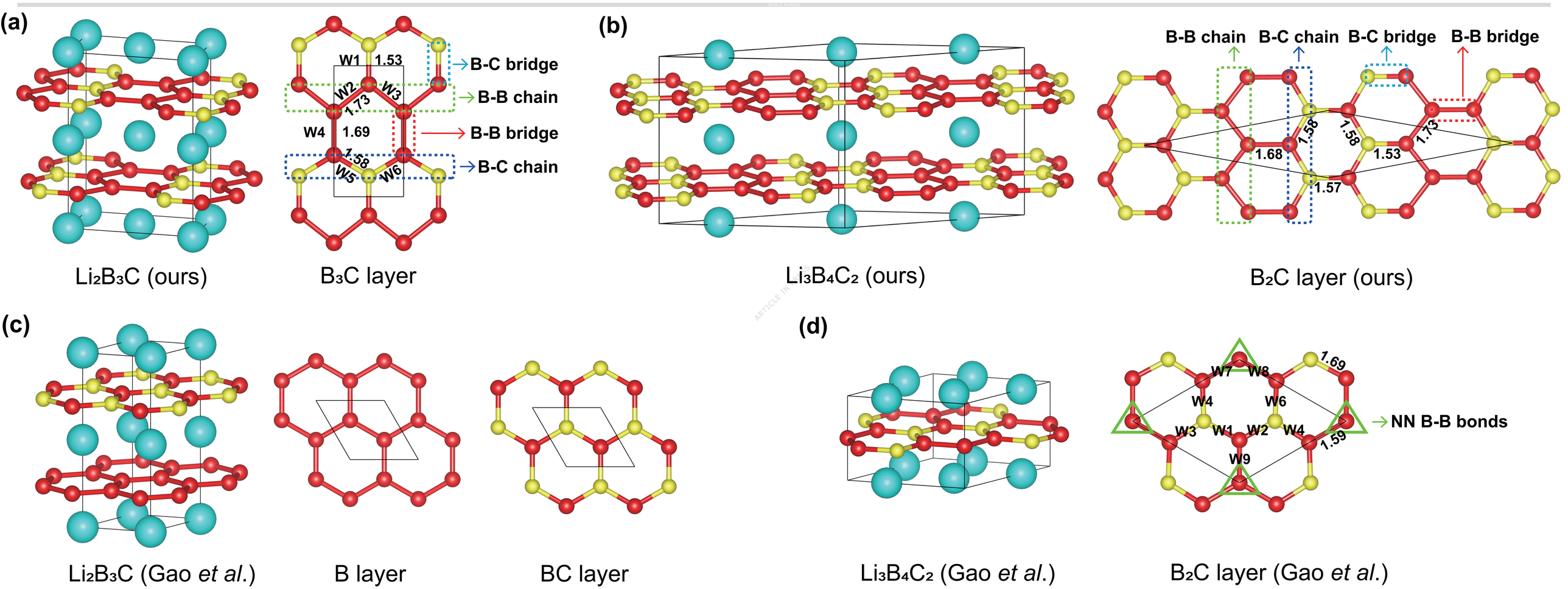
(a)
W1
1.53
W2
W3
1.73
W4
1.69
1.58
W5
W6
B-C bridge
B-B chain
B-B bridge
B-C chain
Li2B3C (ours)
B3C layer
(b)
B-B chain
B-C chain
B-C bridge
B-B bridge
1.68
1.58
1.58
1.53
1.73
1.57
Li3B4C2 (ours)
B2C layer (ours)
(c)
Li2B3C (Gao et al.)
B layer
BC layer
(d)
W7
W8
1.69
W4
W6
W3
W1
W2
W4
1.59
W9
NN B-B bonds
Li3B4C2 (Gao et al.)
B2C layer (Gao et al.)

ARTICLE IN PRESS

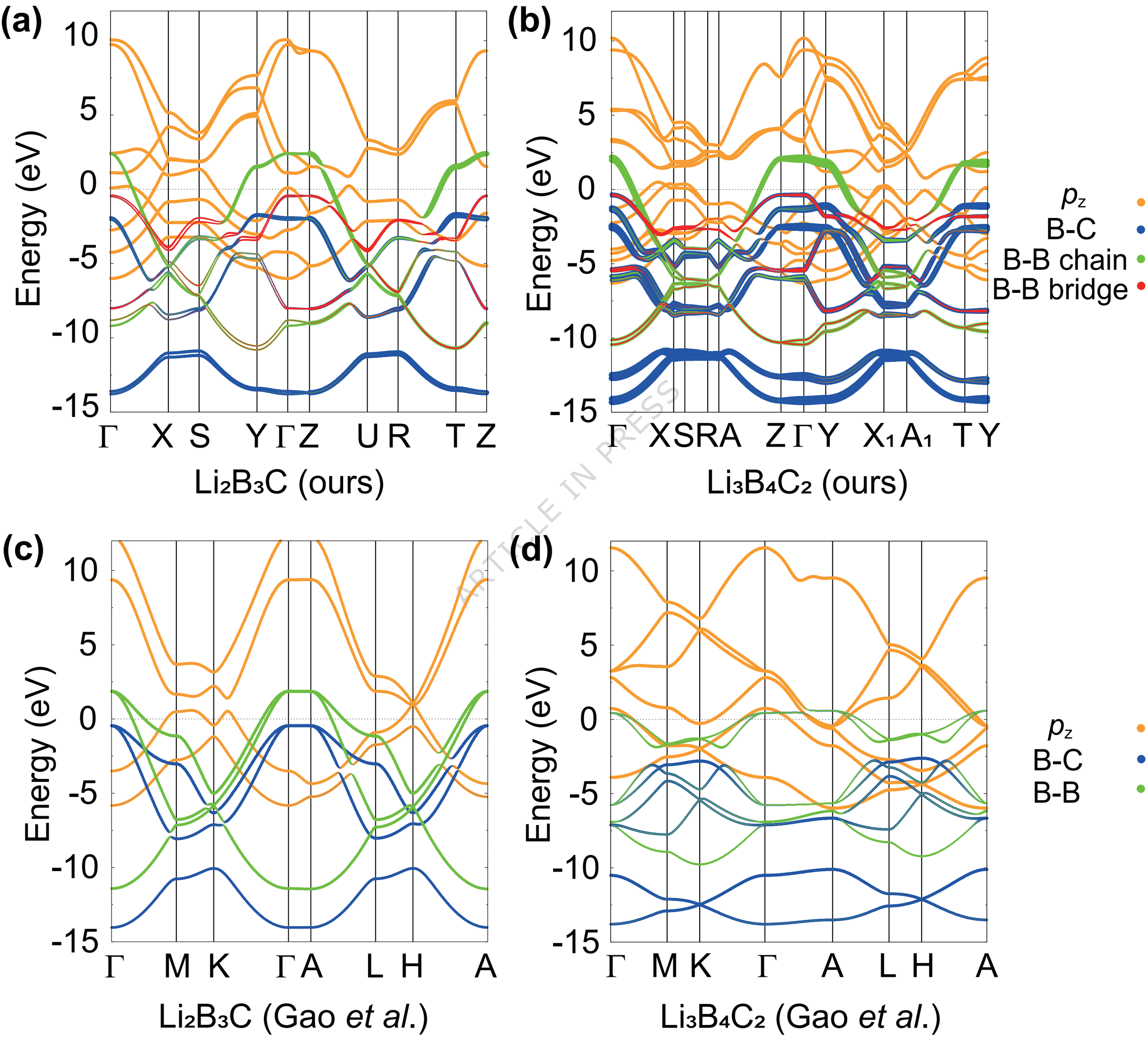

ARTICLE IN PRESS

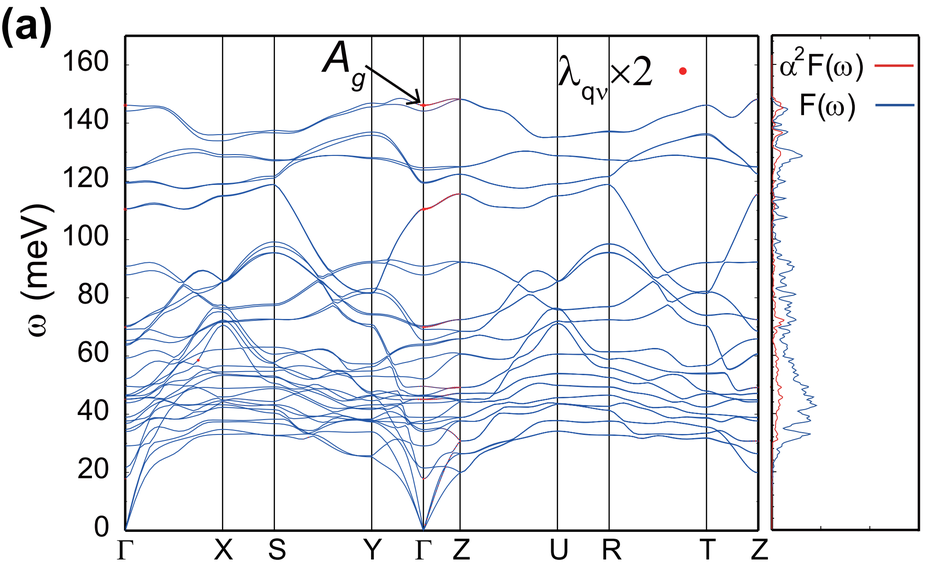

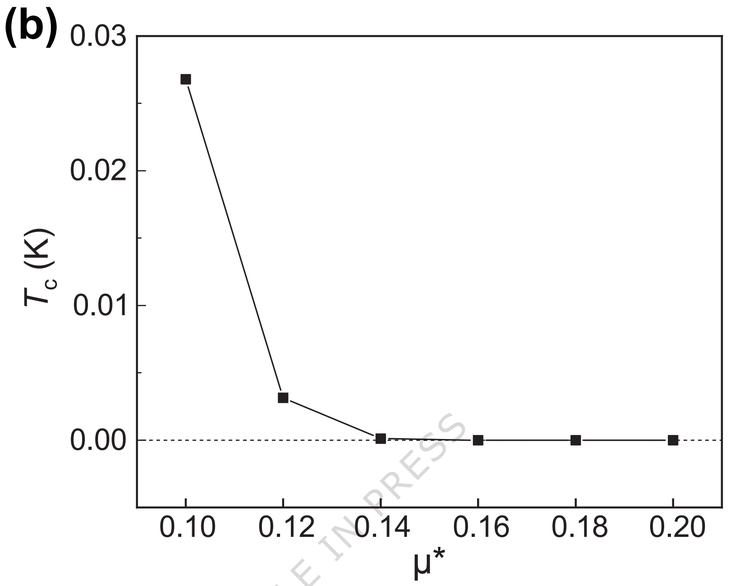

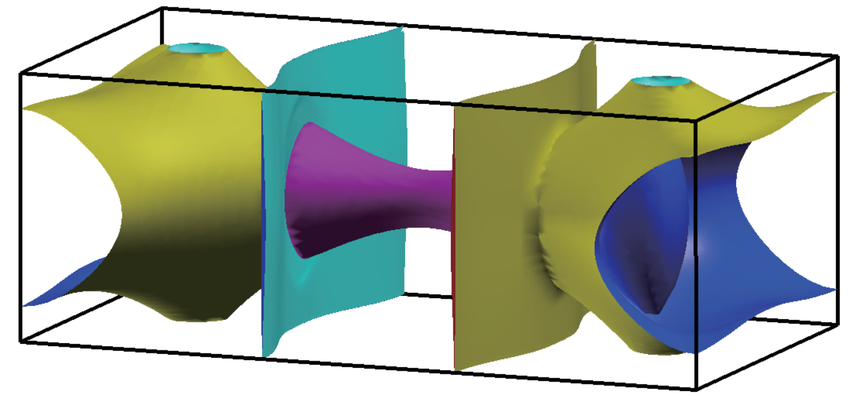

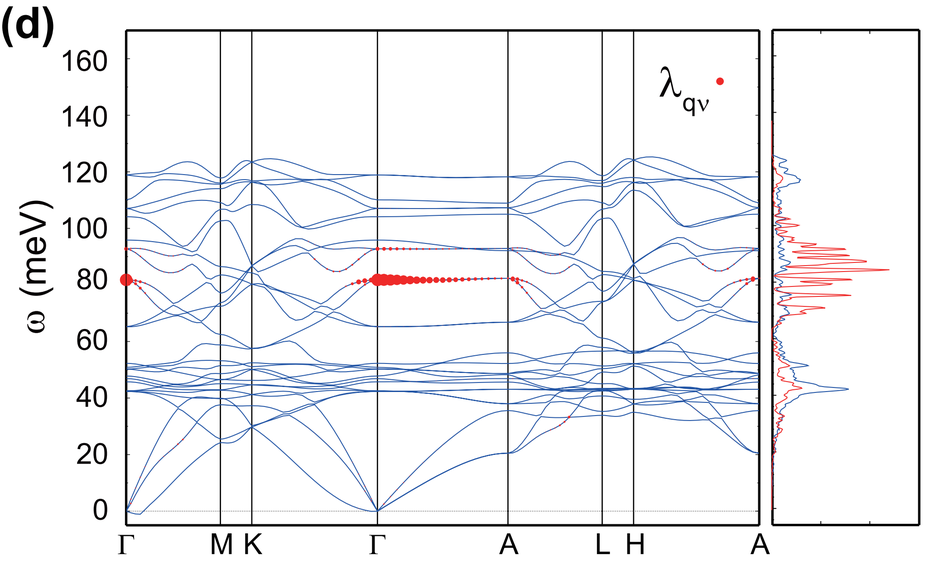

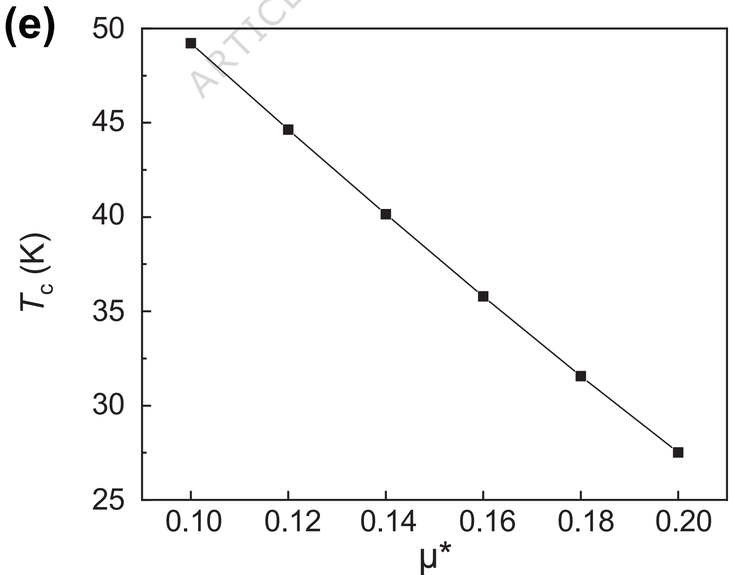

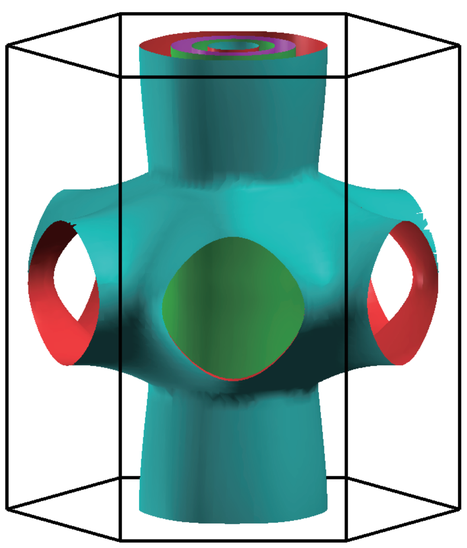

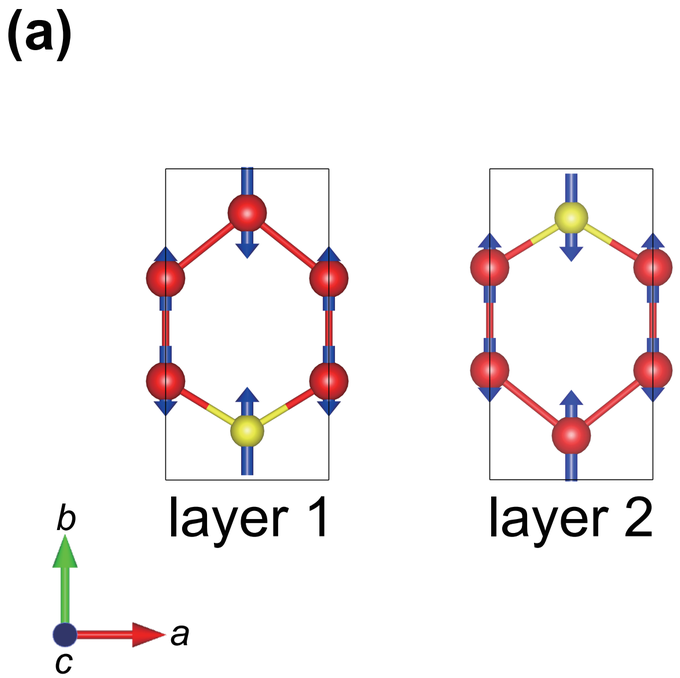
(a)
layer 1
layer 2
b
a
c

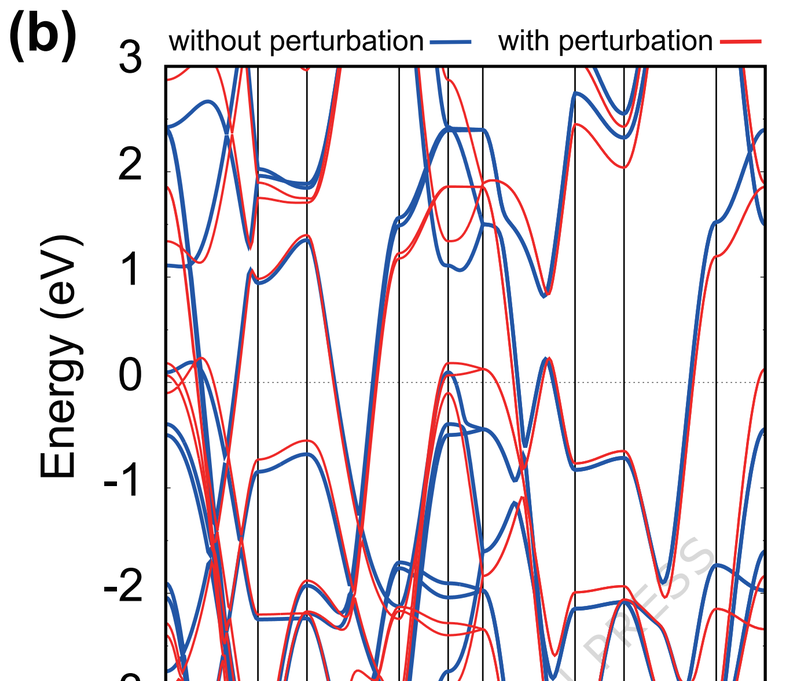
(b)
without perturbation
with perturbation
Energy (eV)
3
2
1
0
-1
-2
-3
Γ X S Y Γ Z U R T Z

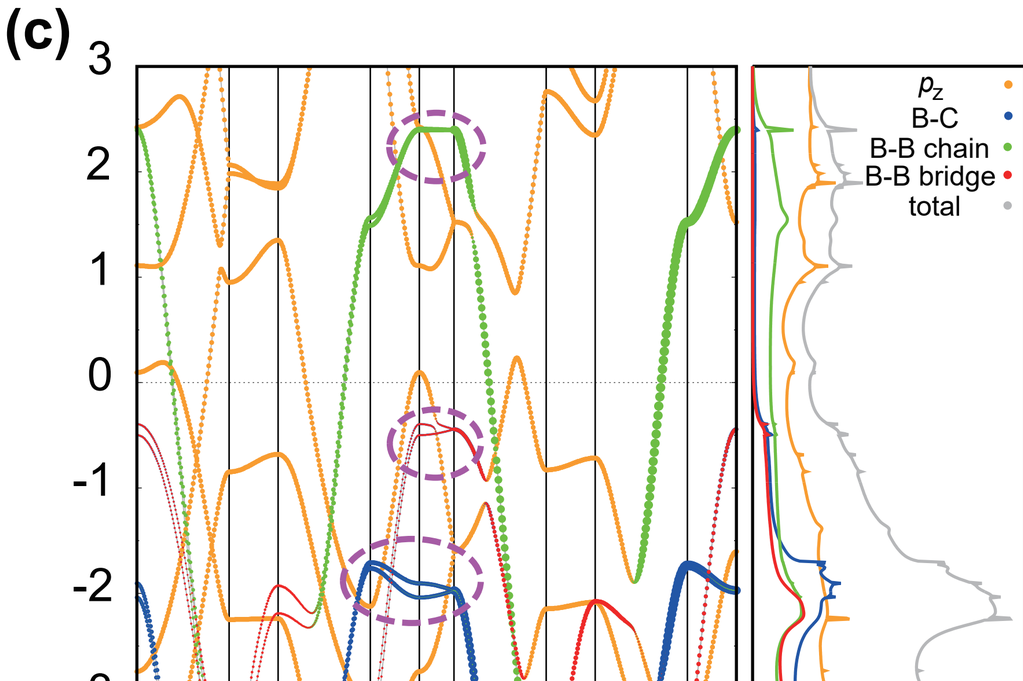
(c)
3
2
1
0
-1
-2
-3
Γ X S Y Γ Z U R T Z
p_z
B-C
B-B chain
B-B bridge
total
DOS

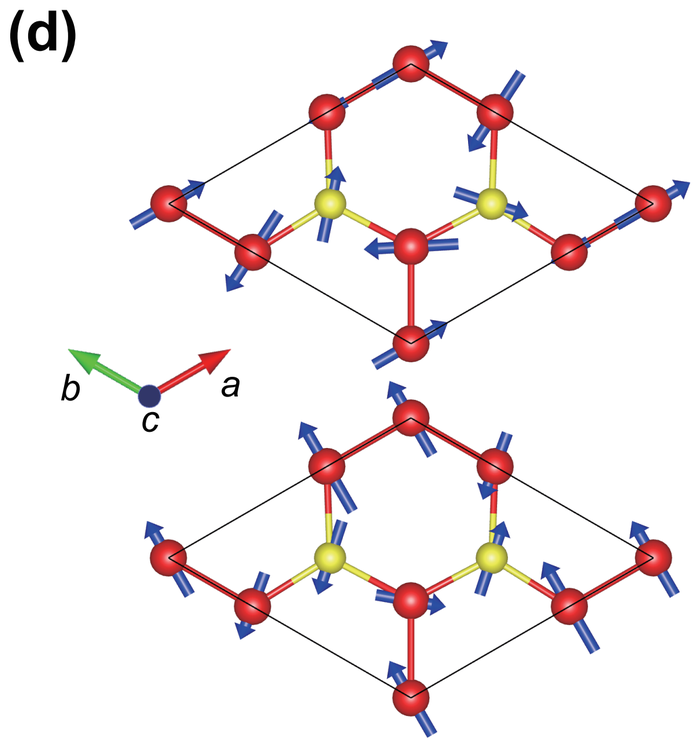
(d)
b
a
c

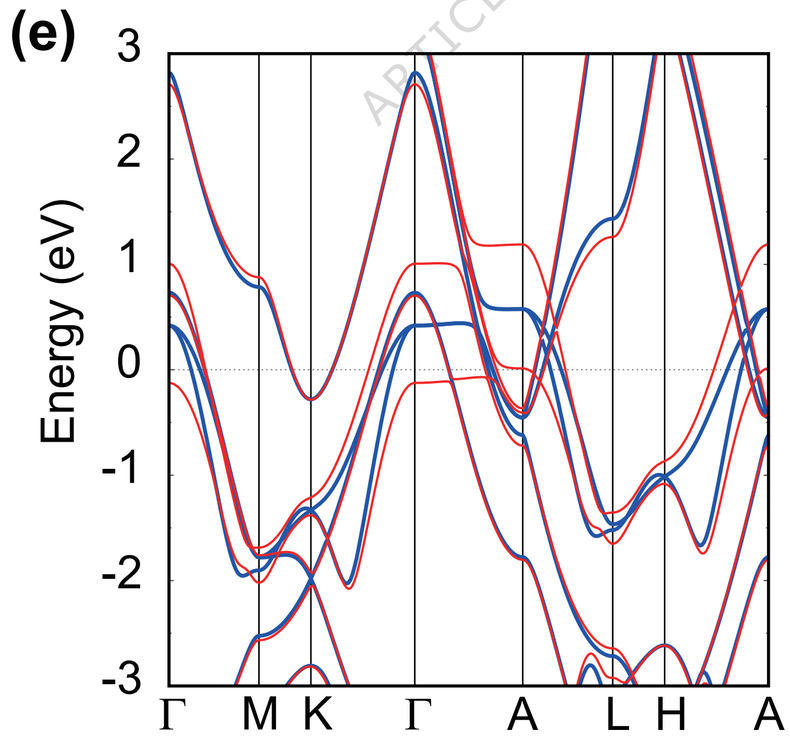
(e)
Energy (eV)
3
2
1
0
-1
-2
-3
Γ M K Γ A L H A

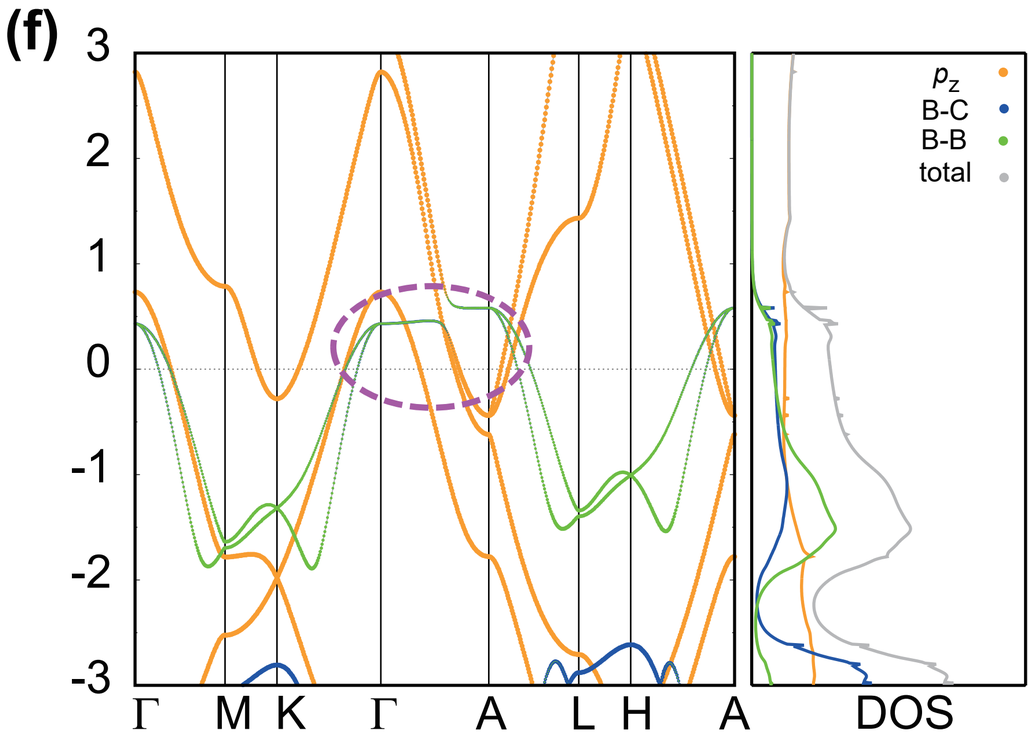
(f)
3
2
1
0
-1
-2
-3
Γ M K Γ A L H A
p_z
B-C
B-B
total
DOS

ARTICLE IN PRESS

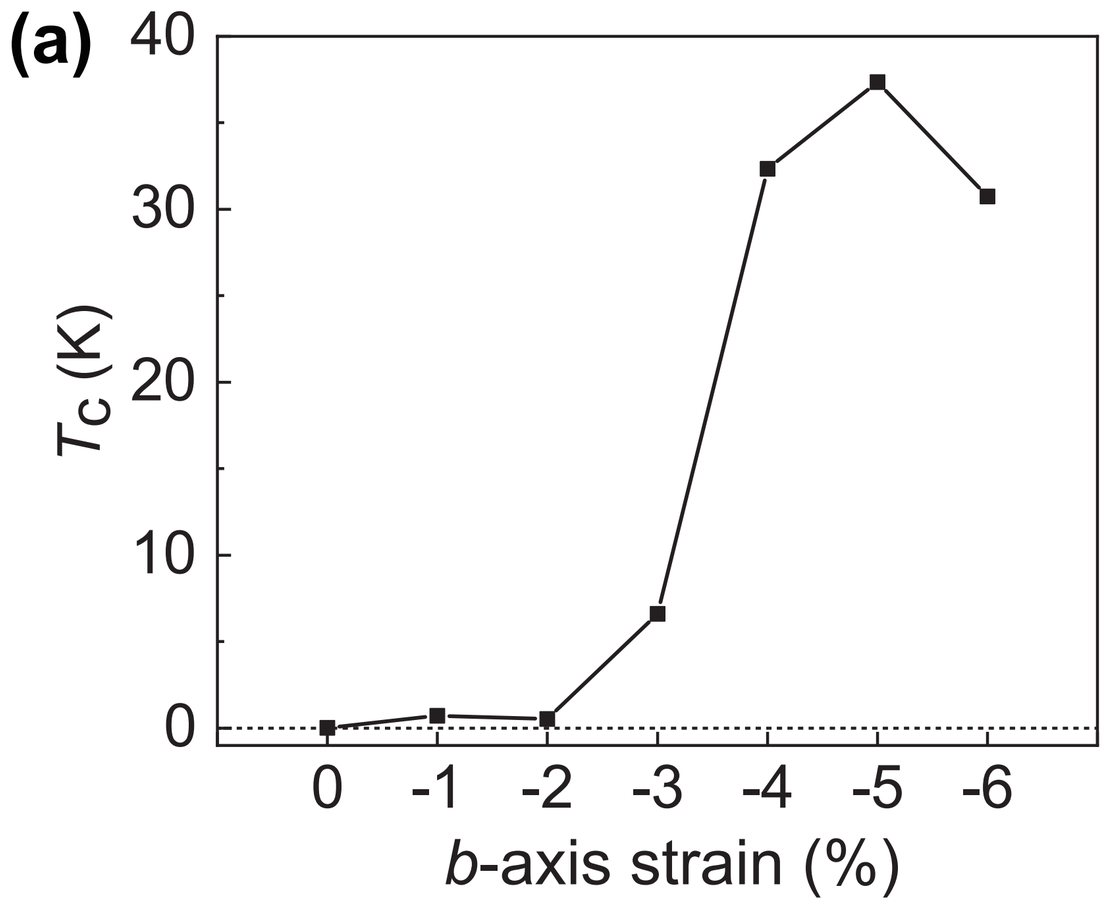

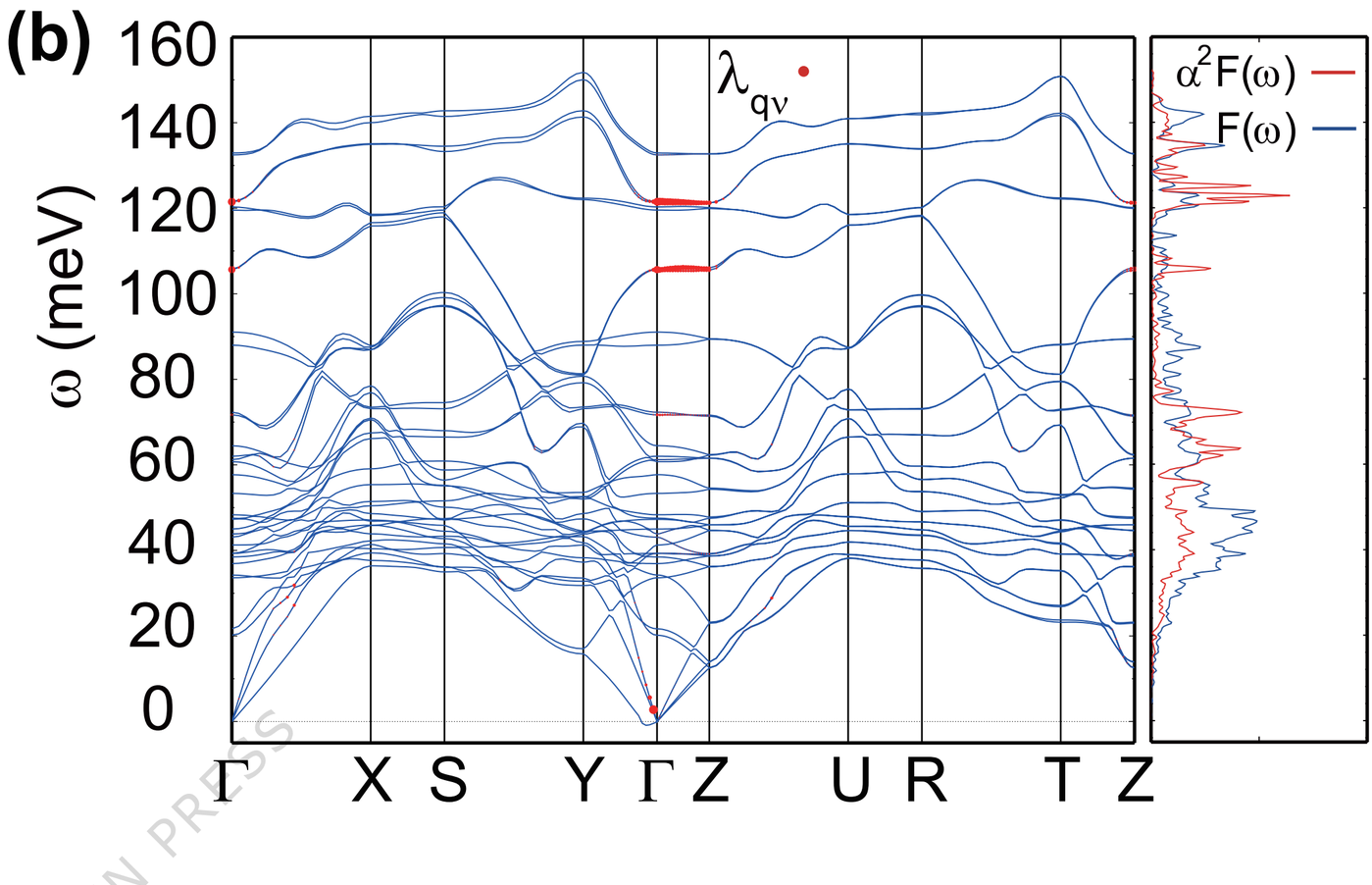

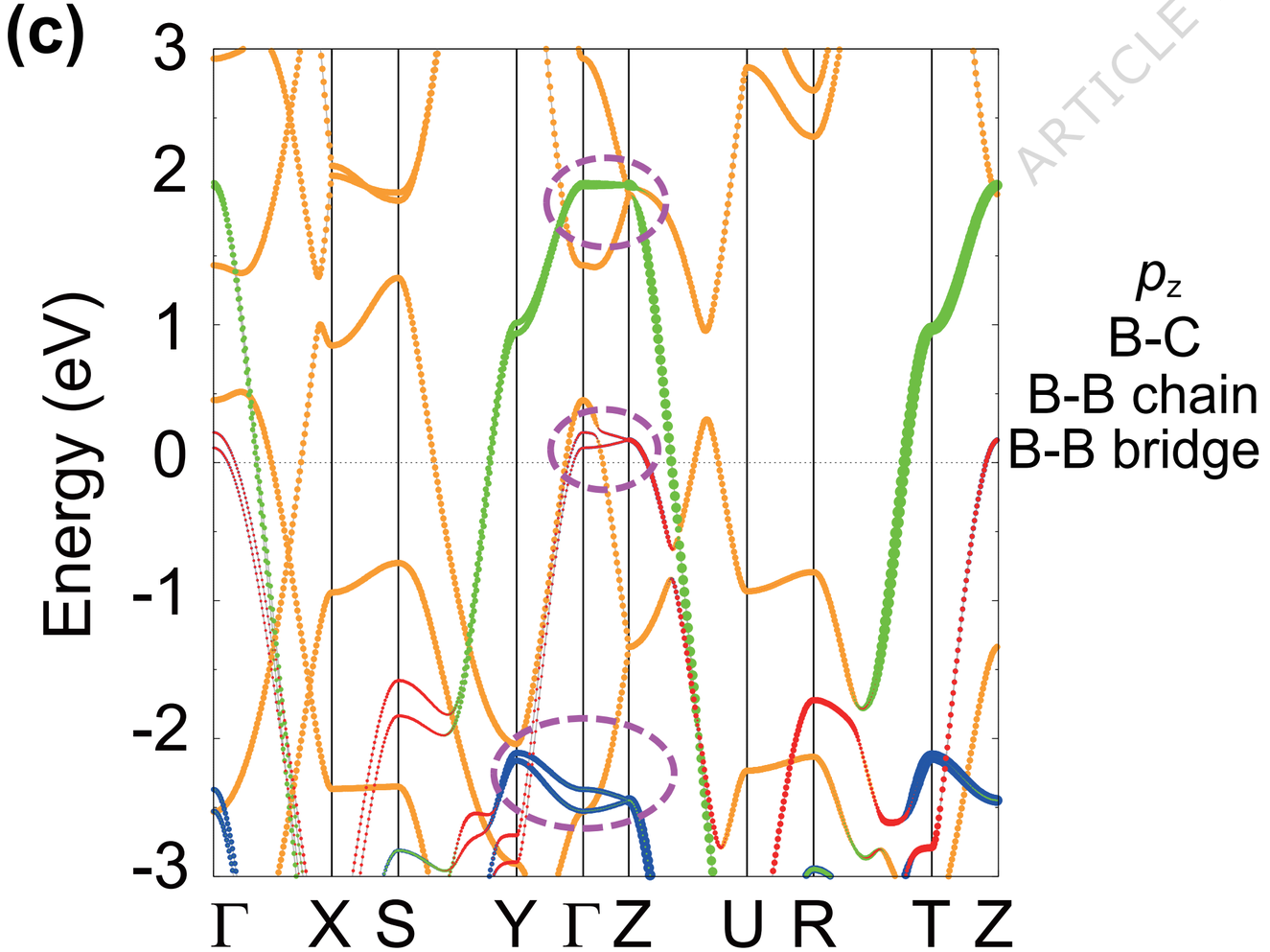

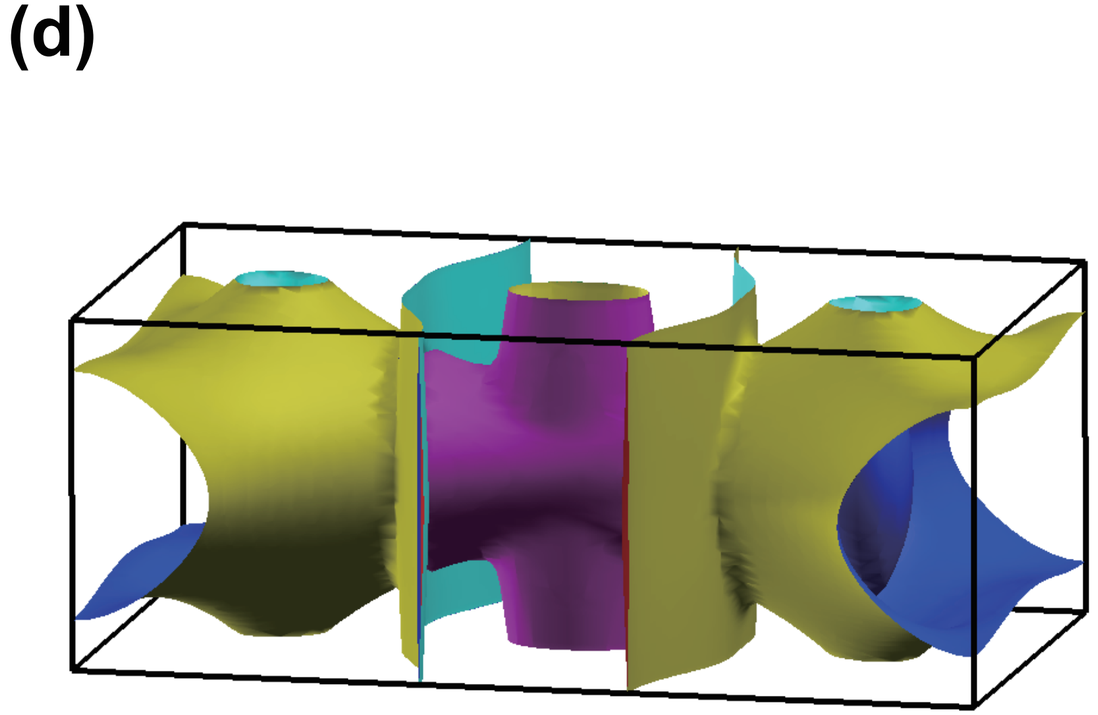

ARTICLE IN PRESS

Boron-rich lithium borocarbides $Li_nB_{n+1}C_{n-1}$ are MgB_2-like candidates for phonon-mediated superconductivity, but the colouring of B/C atoms is unclear. Using first principles calculations, the authors find that Li_2B_3C with optimal colouring and T_c <0.03 K, but −5% uniaxial compression boosts electron phonon coupling and raises T_c to ~37 K.

ARTICLE IN PRESS